Integrated System and Component Technologies for Fiber-Coupled MM-Wave/THz Systems

by

Alireza Zandieh

A thesis
presented to the University of Waterloo
in fulfillment of the
thesis requirement for the degree of
Master of Applied Science
in
Electrical and Computer Engineering

Waterloo, Ontario, Canada, 2012

I hereby declare that I am the sole author of this thesis. This is a true copy of the thesis, including any required final revisions, as accepted by my examiners.

I understand that my thesis may be made electronically available to the public.

Abstract

THz and mm-wave technology has become increasingly significant in a very diverse range of applications such as spectroscopy, imaging, and communication as a consequence of a plethora of signicant advances in this field. However to achieve a mass production of THz systems, all the commercial aspects should be considered. The main concerns are attributed to the robustness, compactness, and a low cost device. In this regard, research efforts should be focused on the elimination of obstacles standing in the way of commercializing the THz technology.

To this end, in this study, low cost fabrication technologies for various parts of mm-wave/THz systems are investigated and explored to realize compact, integrated, and rugged components. This task is divided into four phases. In the first phase, a robust fiber-based beam delivery configuration is deployed instead of the free beam optics which is essential to operate the low cost THz photomixers and photoconductive antennas. The compensation of different effects on propagation of the optical pulse along the optical fiber is achieved through all-fiber system to eliminate any bulky and unstable optical components from the system. THz measurements on fiber-coupled systems exhibit the same performance and even better compared to the free beam system. In the next phase, the generated THz wave is coupled to a rectangular dielectric waveguide through design of a novel transition with low insertion loss. The structure dimensions are reported for various range of frequencies up to 650GHz with insertion loss less than 1dB. The structure is fabricated through a standard recipe. In third phase, as consequence of the advent of high performance active device at mm-wave and THz frequency, a transition is proposed for coupling the electromagnetic wave to the active devices with CPW ports. Different approaches are devised for different frequencies as at higher frequencies any kind of metallic structure can introduce a considerable amount of loss to the system. The optimized structures show minimum insertion loss as low as 1dB and operate over 10% bandwidth. The various configurations are fabricated for lower frequencies to verify the transition performance. The last phase focuses on the design, optimization, fabrication and measurements of a new dielectric side-grating antenna for frequency scanning applications. The radiation mechanism is extensively studied using two different commercial full-wave solvers as well as the measured data from the fabricated samples. The optimized antenna achieves a radiation efficiency of 90% and a gain of $18dB$. The measured return loss and radiation pattern show a good agreement with the simulation results.

Acknowledgements

I would like to express my sincere gratitude to my supervisor, professor Safieddin Safavi-Naeini, for his wisdom, valuable comments, and positive attitude. His valuable directions helped me to flourish my talents in a variety of areas.

A special thanks to Dr. Daryoosh Saeedkia for providing me with keen insight in THz field of study. His company, TeTechS Inc., supports for the first part of the presented thesis.

I also would like to thank Dr. Mohammed Basha for his collaboration on fabrication of my devices.

I am also indebted to my friend and colleague, Ahmed Shehata Abdellatif, for his guidance and encouragements during my research projects.

Last but not least, special thanks to my dear family for their nonstop love and support. I am incredibly grateful for my wonderful family.

This research was supported by National Science and Engineering Research Council (NSERC) of Canada and Research In Motion (RIM).

Dedication

This work is dedicated to my family

for their never ending love and supports.

Table of Contents

List of Tables

List of Figures

Chapter 1

Introduction

1.1 Motivations

Nowadays, fast growing THz and mm-wave technologies play a significant role in a wide range of applications. This technology opens up new opportunities for spectrometers as the spectral fingerprints of a variety of important biological, pharmaceutical, environmental hazardous, and explosives, etc. materials fall in THz rang of frequency. THz spectroscopy has many application in chemical biosensing [1], food monitoring [2], manuscript recognition [3], recycling, monitoring polymeric compounding processes [4] and so on. Additionally, as THz waves penetrate in a broad range of materials, THz imaging brings the opportunity of inspection for desired materials even if they are covered with an opaque packaging; accordingly, the technology can be applied in ubiquitous security systems in different locations such as airports [5]. Furthermore, ever increasing demand on the high speed wireless communication systems forces the current technology toward the higher carrier frequency. Consequently, a huge amount of research has been carried out on the mm-wave wireless communication technology over the last decade. The attraction has been drawn toward THz frequencies to fulfil requirements of ultra-high speed communication applications. The initial results have demonstrated the feasibility of the systems at speeds higher than $100Gb/sec$ [6, 7] whereas further investigation is essential in this field.

The first step to develop a system for aforementioned applications is to integrate the THz source into the rest of the system. Over the past several decades, a wide range of concepts have been applied to generate THz signal. The bulky and expensive THz sources such as Back-Wave Oscillator (BWO) are exclusively for research and experimental pur-

poses. They are complex and expensive and can generate a high power THz signal [8]. On the other hand, low power THz sources are more appealing for commercial devices. Among them, Quantum Cascade Lasers (QCL), frequency multipliers and photonic-based sources are well-known [9]. QCLs cannot cover the whole THz frequencies especially less than 1THz which is more interesting for spectroscopy applications [9]. Even for higher frequencies, the main drawback is low temperature operation for both CW mode [10] and pulse mode [11]. However, the operating temperature can be improved through employing very high magnetic field [12]. The main advantage of photonic-based sources compared to the frequency multipliers is the ability to realize frequency tunability and generation of the THz pulse which are crucial for a wide range of applications [13]. Furthermore, high cost of frequency multipliers make them inappropriate for commercial devices.

The photonic-based sources are conventionally operated by optical beams. The optical part strongly affects other parts of the system and therefore should be the subject of extensive investigation for realizing aforementioned low-cost/complexity integrated THz devices. To realize the photonic part, various ideas have been applied. In the most of the laboratory setups, the free beam optics is employed as no concern exists for compactness and robustness of the setup. However, to improve the stability of the system, the optical part can be replaced by photonic integrated circuits to develop a complete integrated THz system. The other alternative is to deliver optical beam through optical fiber to enhance the robustness of the system.

The unprecedented progress in electronics technology has provided a unique opportunity for novel applications in mm-wave and THz frequencies [14].In the last decade, the advent of amplifiers and active devices at higher frequencies has been a motivation for developing new structures in THz frequencies. In the most of the applications, a THz emitter is a fundamental part of the system. Many on-chip devices have been reported to this end although their main drawback, which is the low efficiency of these technologies, still exist. The other idea is to deploy a hybrid integration through combination of the active and passive structures. Through examining the proposed structures, some components seem to be essential for such a hybrid system. In the first stage, the THz source should be integrated into the system through an appropriate method with the lowest insertion loss. In ref [15], a uni-travelling-carrier (UTC) photodiode based photomixer chip is connected to the circuit using flip-chip method whereas this technique is not applicable at higher frequencies. In addition, some other structures have been reported but their target is not an integrated system. The second crucial part in the hybrid systems is the antenna to radiate THz energy for different application such radar and imaging. As opposed to the

on-chip antennas, off-chip antennas result in cheap and high efficient devices. Finally, as result of low power generated by THz source and high lossy propagation of the millimetre and THz wave in free space, an amplifier is integrated into RF front end.

1.2 Objectives

The main objective in the presented thesis is to investigate different components for an integrated THz or mm-wave system which are shown in Fig. 1.1. Although the operating frequency of all the components investigated in this thesis might not be same, the investigation demonstrates the feasibility of the idea for application in high performance sub-mmW/THz system. The whole contribution in this system is divided in four sections: realizing the optical part of this system using fiber optics, integration of the THz source to a low loss waveguide, integration of the active devices such as amplifiers to the waveguide and finally designing a high efficient antenna to radiate the power. These parts are represented by dashed circles in Fig. 1.1.

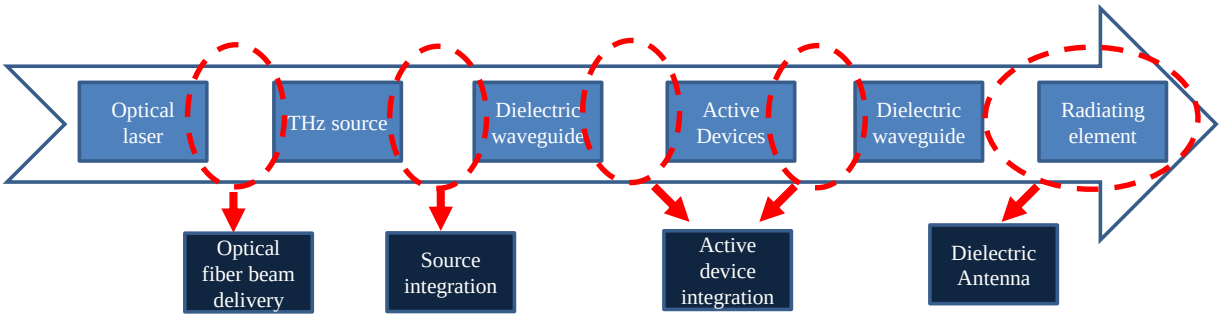

Figure 1.1: Different components for an integrated THz or mm-wave system. The dashed circles show the contributions in the presented thesis.

Referring to Fig. 1.1, in the first part, the main goal is the delivery of a high power short optical pulse of the optical laser after propagation through the fiber to the photoconductive antennas and generating THz signal. The main contribution is development of an all-fiber system for compensation of all effects originating from propagation of pulse through fiber. In the next step, as a hybrid system should be developed, the coupling of the THz wave generated by photonic THz source to a low loss dielectric waveguide is investigated. To this end, a transition with low insertion loss is presented by high-level

modeling of the THz source structure. Then, a highly efficient transition to active device is designed to enhance the power budget of the system. The main goal is to present an efficient transition for active devices with CPW port in sub-mm-wave and THz range of frequencies to a low loss dielectric waveguide. Finally, in the last part, I present a highly efficient antenna on a silicon platform with optimized gain and bandwidth.

1.3 Thesis Organization

The structure of the current thesis is based on the aforementioned components required for realizing a low-cost integrated mm-wave/THz system. The essential background is mentioned at the beginning of each chapter and the rest of the chapter is dedicated to the proposed structure and results.

Chapter 2 will discuss the fiber-coupled system and the related issues. The theory of the pulse propagation is discussed and verified by numerical simulation. The compensation method and the related measurement setups are explained. The THz measurements are performed to verify the performance of the system.

Chapter 3 will focus on design of a transition from photomixer structure to a dielectric waveguide. The design and simulation results are presented and the fabrication process is described. Finally, the fabricated devices are demonstrated in the final section of the chapter.

Chapter 4 is mainly about the integration of the active devices to a low loss dielectric waveguide. Two different structures are proposed for mm-wave and THz frequency range. These structures can meet the challenges associated with this range of frequency. The devices for mm-wave transition are fabricated.

In chapter 5, a highly efficient antenna is proposed for mm-wave and THz applications. The radiation mechanism is discussed comprehensively and verified through various simulations, and the structure is fabricated. The performance of the antennas are verified through the comparison of the simulated and the measured results, respectively.

Chapter 2

THz Signal Generation and Detection Using All-Fiber Beam Delivery

2.1 Introduction

As a consequence of recent progresses in THz area and revealing the potentials of this technology, academic research groups and industries have started to remove obstacles for commercialization of THz systems. One major problem for any system operated by optical beams is the stability, robustness, and ease of handling as a very fine adjustment is required for free space optical setups. The idea of replacing the free beam path with optical fiber in the measurement setups has been considered for many years. Recently some fiber coupled THz systems have been reported for various applications such as spectroscopy [4, 16, 17, 18], biomedical [19], and imaging [20].

In Continuous Wave (CW) THz fiber-coupled systems [21], the main problem that should be addressed is how to focus the output of the fiber on photoconductive antennas; however, in pulse systems [4, 16, 17, 19, 20], the propagation of the high power optical pulse in the fiber should be investigated as well. The main focus of this chapter is the pulse systems.

As a consequence of high efficient materials for generation and detection of the THz pulse using optical beam at $800nm$, most of the proposed systems are operated at this wavelength. However, the systems at $1.55\mu m$ wavelength are more preferable as optical

devices developed for optical telecommunication systems are available at much more reasonable price. Additionally, the compensation technique in the proposed structures to deliver a femto-second optical pulse after propagation through the fiber is based on either free space setups such as grating structures [17] or some modifications in the internal part of the laser structure [16]. Therefore, new methods are essential for optical beam delivery to realize more robust systems.

This chapter proposes a fiber-coupled THz system with the optical pumping at $1.55\mu m$ wavelength for generating THz pulses. In the first section a background is provided on THz measurement configurations especially for pulse operation. Then, the nonlinear effects inside the optical fiber is investigated and verified through numerical simulation. In the next section, the compensation method is discussed in details. The main novelty of this system is associated with the configuration of the system and realizing of an all-fiber system starting from generation of the optical pulse and ending with its focusing on the photoconductive antennas. Finally the THz measurements are performed to verify the high quality of the compensated pulses and the performance of the system. All the measurements are conducted through collaboration with TeTechS Inc. to obtain reliable results.

2.2 Background

A variety of techniques are employed for generating THz signal using optical signal. A basic mechanism is to down-convert the optical signal to THz frequency range. To generate continuous-wave (CW) THz signal, a well-known photomixing technique leads to simplest implementation and is suitable for commercial devices. In this method, two laser beams with frequency difference equal to desired THz frequency illuminate a dc-biased non-linear material such as GaAs, LT-GaAs, and InGaAs [13]. The optical beams can originate either from a dual-mode laser or two synchronized single-mode lasers. The output THz frequency can be tuned by slightly varying the wavelength of the lasers.

However, in pulse mode, instead of two optical beams, an ultra-short optical pulse illuminates the structure to generate a THz pulse with an spectral bandwidth up to $4THz$. As a consequence of higher output power in pulse mode, this technique is more attractive for commercial devices, particularly those which need a very wide-band THz signal.

2.2.1 Free Space Pump-Probe THz Measurement

Pump probe THz measurement is a well-known technique for different applications such as spectroscopy. Since the proposed fiber coupled system is designed based on this method of measurement, this section provides a brief explanation on generation and detection of the THz pulse and the whole system in general [22]. The same concept is applied for the CW THz generation and detection.

To generate THz pulse a static electric field is created by applying a dc bias voltage across two metal strips on a non-linear medium. The bias voltage depends on the gap size between the two metals as the maximum electric field is limited by the break down field threshold. Then, this region is illuminated by the optical pulse to generate the free electron and holes. The energy of the incident photons should be greater than the band gap of the non-linear medium to excite electrons from valance band to conduction band. The created free electrons and holes accelerate in electric field in opposite directions and generate a current in the region close to the surface of the substrate. The current generates THz pulse and radiates it to the free space. To improve the power of the generated THz signal, an antenna structure is implemented on the substrate to couple THz wave to free space more efficiently. Moreover, an additional high-resistivity silicon lens is attached on the backside of the substrate to reduce the reflection from air-dielectric interface [23].

The same physical principals are applied to detect an incident THz pulse. The metal strips are connected to a current meter. Both THz pulse and optical pulse are illuminated over the gap between the metal strips. The role of the optical pulse is generation of the free carriers in the non-linear substrate to increase the conductivity at the specific time intervals. Depending on the delay between optical pulse and THz pulse, a particular part of the THz pulse arriving on the surface of the substrate, induce the voltage over the metal strips, and generate the current which is measured by the current meter. Through changing the delay between two pulses, the THz pulse is sampled in time and characterized. The time resolution relies on both the material properties of the photoconductive structure and the incident optical pulse. To clarify this point, a very low carrier life time and a very short optical pulse result in very fast change in the gap resistance form insulating to conducting. Similarly, the silicon lens and antenna structure have significant effects on enhancing the efficiency of the system.

The measurement setup is shown in details in Fig. 2.1. As mentioned, to conduct THz pump-probe measurement, two optical beams are required to excite carriers in photocon-

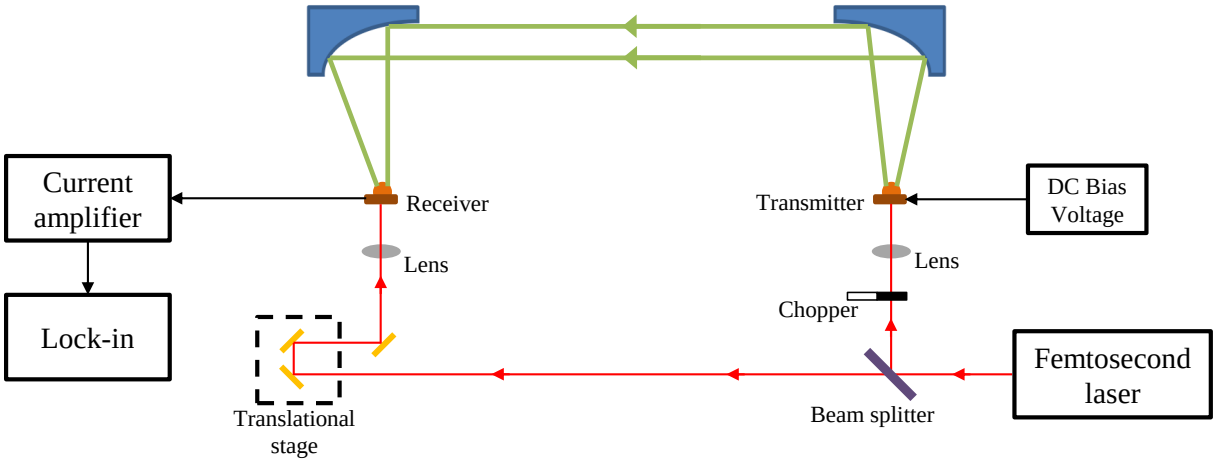

Figure 2.1: The pump-probe measurement setup for THz generation and detection

ductive antennas. To this end, the femto-second optical pulse coming from the laser is split to two beams by beam splitter. One beam hits to the transmitter photoconductive antenna which is biased to generate THz signal, and the other one propagates through a combination of the mirrors to reach to the receiver photoconductive antenna. THz pulse propagates in free space through the parabolic mirrors as no lenses exist at THz frequency similar to highly efficient optical ones. The optical mirrors are on a translational stage to provide an arbitrary time delay between arrival of the THz pulse and optical pulse to the receiver antenna. Two lenses are mounted close of the antennas to accurately focus the optical beams on the antenna gaps. The chopper is utilized as a low-frequency amplitude modulator because the measurement is performed by lock-in amplifier to eliminate $1/f$ noise at low frequencies. The output of the receiver antenna goes to low-noise current amplifier to improve the SNR of the measurement.

2.2.2 Fiber-Based Pump-Probe THz Measurement

As shown in Fig. 2.2, in fiber-coupled setup, all free space optical parts are replaced with the optical fiber. Consequently, a fiber pigtailed pulse laser usually is utilized. The fiber splitter provides two required optical pulses. A length difference should be realized between the arms to compensate free space propagation of the THz pulse. Based on this configuration, the delay line cannot be realized in optical path; accordingly, to provide the desired delay, the whole receiver or transmitter part should move to change the dis-

tance which THz pulse propagates through. The lock-in measurement is still preferable; therefore, the chopper should be mounted in such a way to modulate THz beam instead of optical beam. A better idea is to chop the bias voltage to remove the mechanical chopper through applying a square wave voltage over the antenna gap.

To focus the optical beam on the antennas, the fiber can be directly attached to the antenna gap to remove any optical components. However, as a proof of concept, the output pulse of the fiber can be focused on the antenna by a beam collimator and a lens. Additionally, in the absence of the fiber pigtailed laser, at the initial stage, the laser beam can be coupled to the fiber using an objective lens with the appropriate numerical aperture.

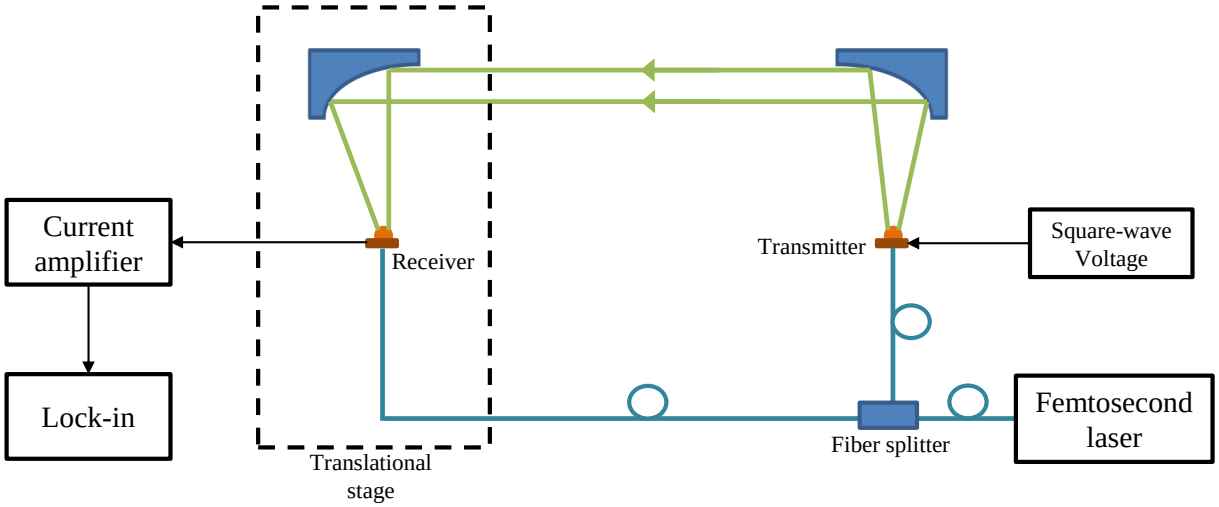

Figure 2.2: The fiber-coupled pump-probe measurement setup for THz generation and detection

The main challenge in developing a fiber-coupled system is the delivery of a femtosecond pulse to the antennas after propagation through the optical fiber. In fact, many phenomena exist in optical fiber that affect the pulse properties and especially the pulse shape. These effects are critical even after very short length propagation of the high power and very short width pulse. The main focus of this chapter is to understand these effects, compensate them, and show the feasibility of the THz pulse generation using the optical fiber for beam delivery.

The idea of all-fiber optical beam delivery in THz systems opens up the opportunity of commercializing the THz systems due to a number of advantages. The main bottle neck of the free beam optical system is the accurate alignment needed before the operation. This situation is even more critical for portable devices. The fiber-based system is very robust and stable and no alignment is required. Furthermore, the system would be more compact as the bulky optical components are eliminated from the system. Finally, the fiber-coupled system exhibits more flexibility in terms of measurement type. For instance, in THz spectroscopy systems, the measurement setup can easily be converted from transmission mode to reflection mode as no alignment is required for optical path.

2.3 Nonlinear and Dispersion Effects Related to the Ultra-Short High Power Pulse Propagation in Fiber

2.3.1 Theory

The propagation of the optical pulse along the fiber is governed by non-linear Schrodinger equation:

$$i\frac{\partial U}{\partial z} = \frac{sgn(\beta_2)}{2L_D}\frac{\partial^2 U}{\partial \tau^2} - \frac{\exp(-\alpha z)}{L_{NL}}|U|^2 U \tag{2.1}$$

In this equation, U is the normalized amplitude and τ represents the time which is scaled by pulse width [24]. The right hand side of this equation can be split in two parts. The first part is associated to the linear dispersion leading to pulse broadening while the second part is related to the nonlinear effects originating from intensity dependent refractive index. These terms are scaled by dispersion length L_D and nonlinear length L_{NL}, respectively [24]. These two parameters are defined as follows:

$$L_D = \frac{{T_0}^2}{|\beta_2|} \tag{2.2}$$

$$L_{NL} = \frac{1}{\gamma P_0} \tag{2.3}$$

These two length scales are measured of dispersion and non-linearity in propagation of the pulse through a particular length. The dispersion length is a function of the pulse

width (T_0) and the second derivative of the propagation constant β_2 which is the indication of the dispersive behavior of the fiber. On the other hand, the nonlinear length is inversely proportional to the pulse peak power (P_0). Furthermore, the nonlinear length depends on the (γ) which is defined in Eq. 2.4 [24], where c is the light velocity and ω_0 is the instantaneous frequency. A_{eff} is the effective area of the fiber cross section where most of the pulse energy is confined in.

$$\gamma = \frac{n_2 \omega_0}{c A_{eff}} \tag{2.4}$$

In Eq. 2.4, n_2 originates from the non-linear effects. To clarify, non-linearity mainly result in self-phase modulation. Owing to this phenomenon, the refractive index of the fiber depends on the electric field intensity based on Eq. 2.5:

$$\tilde{n}(\omega, |E|^2) = n(\omega) + n_2 |E|^2 \tag{2.5}$$

The parameter N is defined in the Eq. 2.6:

$$N = \frac{L_D}{L_{NL}} \tag{2.6}$$

This parameter provides a criteria for the significance of the different mechanisms in propagation of the pulse along the fiber. Therefore, if $N \gg 1$ which means $L_{NL} \gg L_D$ the nonlinear effects can be neglected and the opposite happens when $N \ll 1$ ($L_{NL} \ll L_D$). In a special case where both L_{NL} and L_D are much larger than the fiber length the output of the fiber is exactly the input pulse since the two terms on the right hand side of the Eq. 2.1 goes to zero if a smooth temporal profile is assumed for the optical pulse. The interesting case happens when N is neither too high nor too small. Both effects should be considered for this case which usually exists for femto-second pulses with very high peak power.

Apparently, the effect of the dispersion is the broadening of the input pulse either in normal dispersion regime or anomalous dispersion regime. However, to understand the effects of the nonlinearity on the input pulse, the solution of the aforementioned equation can be found when no dispersion contributes to the pulse evolution; or equivalently, the dispersion length is infinite. In this case, the analytical solution for Eq. 2.7 is obtained as follows [24]:

$$U(L, T) = U(0, T) \exp(i \phi_{NL}(L, T)) \tag{2.7}$$

Referring to Eq. 2.7, the pulse shape is preserved when the nonlinearity is dominant although a nonlinear phase shift (ϕ_{NL}) accumulates as the pulse propagates through the fiber. The nonlinear phase is obtained from following equation [24]:

$$\phi_{NL}(L,T) = |U(0,T)|^2 (L_{eff}/L_{NL}) \tag{2.8}$$

$$L_{eff} = [1 - \exp(-\alpha L)]/\alpha \tag{2.9}$$

where L denotes the length of the fiber. The nonlinear phase is the source of the spectral broadening in absence of the linear dispersion. To clarify, the first time derivative of the nonlinear phase represents frequency chirping which expresses the time dependency of the instantaneous optical frequency. Consequently, new frequency components are created as the pulse propagates. The analytical expression for the the change in the the instantaneous optical frequency over time [24] is:

$$\delta\omega(T) = -\frac{\partial \phi_{NL}}{\partial T} = -(\frac{L_{eff}}{L_{NL}})\frac{\partial}{\partial T}|U(0,T)|^2 \tag{2.10}$$

Based on this relation, as well as the length of the fiber, the frequency chirping depends on the pulse shape itself. Due to the fact that instantaneous frequency variation depend on the first derivative of the pulse shape the leading edge results in negative value whereas the trailing edge causes positive chirp. The unchirped and chirped pulse are shown in Fig. 2.3

However, in the presence of the linear dispersion the mechanism is different. Both nonlinearity and dispersion contribute to pulse propagation and cannot be considered separately. Two different regimes are now considered. In normal dispersion region β_2 is positive which means higher frequency components expose to less propagation delay. Consequently, the leading edge of the pulse propagates faster whereas the trailing edge reach to the end of the fiber with more delay; therefore, nonlinear effects expedite the pulse broadening in normal dispersion regime. On the other hand, as a result of the same sign of the frequency chirp for dispersion and nonlinear effects, pulse spectrum is broadened in frequency domain.

In anomalous regime where β_2 has a negative sign, the dispersion and nonlinearity act in opposite direction. Since higher frequencies of the optical pulse are subjected to less propagation delay, the optical pulse becomes dispersed more slowly. Furthermore, as the

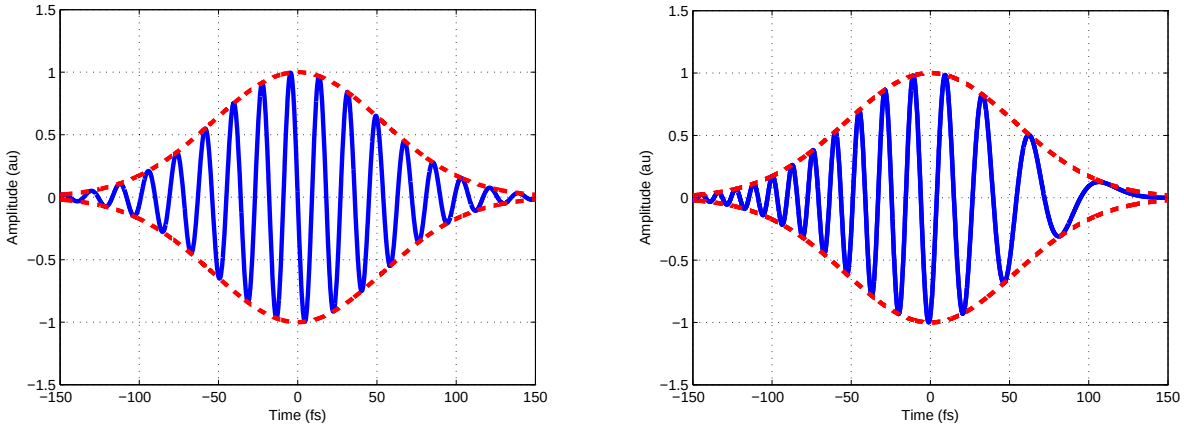

(a) (b)

Figure 2.3: (a) Unchirped pulse (b) Chirped pulse as a consequence of non-linear effects

frequency chirps which originate from dispersion and nonlinearity compensate each other, the optical pulse appears to get compressed in frequency domain.

2.3.2 Numerical Results

The qualitative description provided in last section can be verified by solving the Eq. 2.1 numerically for particular fiber lengths. Numerous methods have been proposed to obtain either precise or approximate solution for Schrodinger equation. Split-step Fourier method provides a very good approximation for the pulse propagation in the presence of the non-linear effects [24, 25]. This method divides the propagation distance into the very small segments. The main assumption is independent action of dispersive and nonlinear effect in each segment. To explain this, in the simplest way, the equation is solved in two steps: first the dispersion is assumed zero and the solution is obtained in time domain for propagation in one segment; in the second step, the nonlinearity is assumed zero and the solution is obtained for dispersive media for propagation in one segment. The segment is solved in frequency domain to use the FFT method which reduces the computational time. In fact, as compared to the finite difference which results in a more accurate solution, this method is much faster [26]. To enhance the accuracy of the method, the segments can be chosen smaller.

Using this method, the variation of the pulse profile for propagation along $2m$ single mode fiber is obtained and represented in Fig. 2.4. The simulation is performed to realize what should be expected in the experiment; therefore, the input pulse has $100fs$ FWHM which is same as the available femto-second pulse in the laboratory. The simulation is for two case of high and low power input pulse to highlight the nonlinear effects in propagation of the pulse. Typical value for fiber parameters is applied in the simulation. Referring to Fig. 2.4, linear dispersion is apparent in low power regime whereas by increasing the input pulse power, the amount of dispersion is reduced considerably since the pulse is at $1.55\mu m$ wavelength (anomalous dispersion regime).

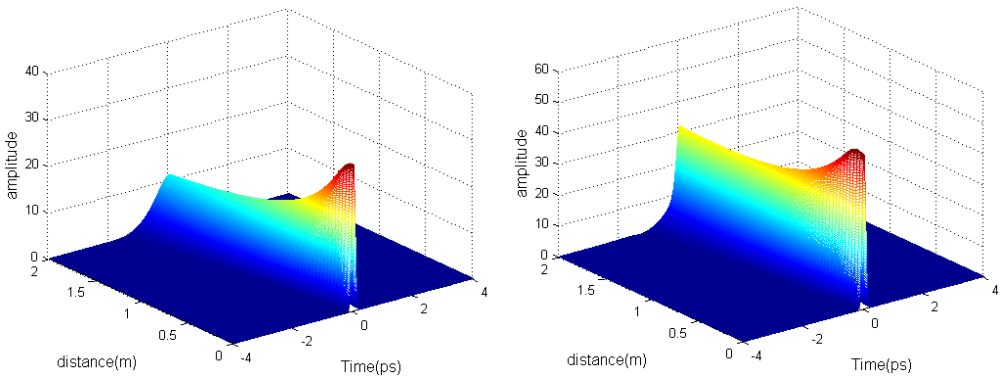

(a) (b)

Figure 2.4: Numerical simulation of the propagation of the optical pulse through 2m fiber (a) Low power input pulse (b) High power input pulse

To represent the dependency of the dispersion on the nonlinear effects, the relative dispersion versus input peak power is plotted in Fig. 2.5. The ratio of the amount of pulse broadening with and without the nonlinear effect is calculated and shown versus peak power. Referring to Fig. 2.5, as a result of increasing the power, the amount of dispersion is much less than what is expected in the absence of the non-linear effects. The simulation results cannot predict the exact values in the experiments as many uncertainties exist in pulse properties. Consequently, these results yield a very good insight to the behaviour of the system.

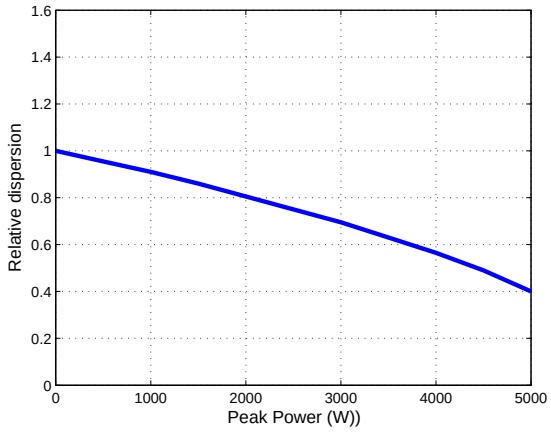

Figure 2.5: Dispersion relative to the absence of the non-linear effects

2.4 Pulse Retrieval

2.4.1 Compensation Method

Several techniques have been proposed for compensation of the fiber dispersion in general. Some of them are based on free beam configurations. In a particular arrangement, the angular dispersion of two grating structures [27] or sequence of prisms [28] can be exploited for generation of negative dispersion. In fact, the first structure disperses the incident collimated beam spatially, and then the second structure collimates the beam. The difference in the distances that the various frequency components travel between two structures is the source of the negative dispersion. Although, the prism pairs are low loss and more convenient for adjusting the sign and the magnitude of the dispersion, the grating structure can provide high amount of negative dispersion. Another low loss structure for dispersion compensation is Gires-Tournois interferometer [29]. In this configuration, a partially reflective mirror is placed against the total reflective mirror to form a resonator. Therefore, the structure shows a frequency dependent behaviour and provides desired dispersion. However, to realize a robust system, any free space beam part such as those in the mentioned methods should be eliminated.

On the other hand, a variety of methods can be applied to compensate the non-linear effects. Conjugating the temporal envelop of the optical pulse [30] can compensate some nonlinear effects. However, in the presence of higher order nonlinearities, the frequency

components of the optical pulse can be conjugated by conjugation of the pulse phase as well as time reversal [31]. In addition, employing some adaptive methods to change the input pulse profile in order to achieve desired output pulse is another successful method for compensation of dispersion and non-linear effects [32]. Different methods for spatial pulse shaping have been utilized to tune the phase and magnitude of the frequency component of input pulse. However, the aforementioned methods add undesirable complexity to the proposed system.

To eliminate any complication and establish a stable system, all-fiber configuration is selected. In this approach, the dispersion compensation fiber is utilized for regeneration of the input pulse shape after propagation through the fiber. Although all effects cannot be compensated by DCF, the best efforts are made to achieve to the shortest pulse. Good results are expected as the input pulse which does not have too high power. The configuration for providing two short pulses is represented in Fig. 2.6. The DCF is at the end part of each arm and is connected to SMF using fusion splicing. This configuration can resolve many issues.

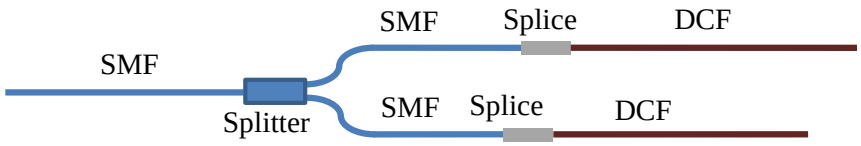

Figure 2.6: The main configuration for providing to short width optical pulses with particular time delay

Single mode DCF suffers from a variety of problems [24]. The propagation of the optical pulses through DCF leads to higher power dissipation which is around $0.5dB/km$. To resolve this problem, less than $10m$ fiber is utilized for the implementation of the system. Moreover, as a consequence of smaller core, the electric field intensity is much higher in DCF core compared to SMF; therefore, the non-linear phenomena are more effective even in low power regime. However, this issue is eliminated by considering a particular configuration in which the lowest power reach to DCF. To this end, to compensate the dispersion and nonlinearities in each arm, although DCF can be inserted in different parts of the system, the end of the arms is the optimum position because of two reasons. First, to reduce the number of the required splices to enhance the power budget of the system. As explained in the next section, each splice introduces noticeable loss to the system. Secondly, to minimize the non-linear effects in DCF as the minimum power in the system is

at the end of the arms.

The dispersion of SFM is $17ps/(nm.km)$ while this parameter for DCF is $-40ps/(nm.km)$. The length of each arm should be chosen carefully due to the fact that particular time delay between output pulses of two arms is required to compensate THz propagation in free space in pump-probe THz measurement setup.

2.4.2 Fiber Splicing

The power budget in proposed system is very crucial and the best effort should be made to eliminate or reduce any sources of power dissipation. In fact, the limited amount of power is available in the fiber pigtailed lasers which are suitable for an all-fiber system. Since the total length of the system is quite short, the fiber losses are of no concern. As a consequence of applying the DCF for shortening the optical pulse, the main optical power loss originates from the connection of SMF to DCF. As explained, a particular configuration is advised to decrease the number of the required splices. Additionally, especial strategies should be employed to reduce the splice loss.

The knowledge of the fiber structure is helpful to understand the mechanisms contributing to the splicing loss. The fiber is made of the silica glass; however, to change the refractive index of different parts, various molecules are doped to the silica glass [33]. Germanium (Ge) and Fluorine (F) are two well-known dopants. Ge raises the refractive index of the silica glass while F lowers it. The refractive index profile of the SMF and the DCF are shown in the Fig. 2.7. Ge is doped in the middle part of SMF to confine the energy in this region. For DCF, an especial profile is required to provide negative dispersion. The core is smaller while a ring around the core is doped by F.

The high insertion loss of the splice can be explained by referring to the refractive index profile of the fibers. Different core sizes and profiles lead to different mode field shapes for these two fibers; consequently, the incident field distributions of the fibers do not match. Additionally, very small core size of DCF results in a high sensitivity of this type of fiber to imperfections. For instance, the angle between the cleaved end faces of the fibers should be less than 1^o for proper splicing.

Different techniques are applied to enhance the quality of the splice. This section focuses on two of them as they are applicable for the current system. It has been shown that

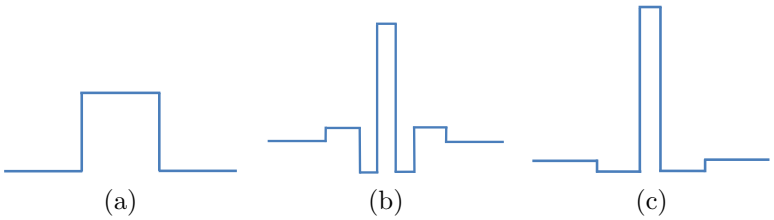

Figure 2.7: Refractive index profile for three different fibers: (a) SMF (b) DCF (c) IMF

applying an intermediate fiber (IMF) leads to the lowest possible loss [34]. This technique employs another type of fiber known as bridge fiber to connect SMF to DCF. The refractive index profile for IMF, as shown in Fig. 2.7, is same as DCF expect that the contrast between regions is lower. Although two additional splices are required in this technique, the insertion loss can be as low as $0.4dB$. However, this method is not appropriate for the proposed system mainly due to introducing more complexity to the system. To explain this, it is noted that the IMF part should be long enough (more than $2m$ or $3m$) to results in acceptable performance. The system with a long length has other issues such as the interaction of the optical pulse with the fiber media which is apparently stronger in longer length.

The other method which has been successfully applied to the proposed system is to exploit thermal diffusion of dopants. This method gives rise to a higher insertion loss but the implementation is more suitable for our system as no extra components are required to be added. At high temperature such as fusion temperature, the dopants start defusing from the regions with higher concentration to the region with lower concentration. The diffusion rate depends on the contrast of the concentration in different region. Higher contrast results in more rapid diffusion; therefore, this effect is considerable in DCF. Depending on the heat source configuration, the diffusion of the dopants changes the profile and can improve or aggravate the quality of the splicing. In fact, if the heat source for fusion splicing is distributed in an appropriate way, this phenomenon provides a tapering section between two different profile and reduce the insertion loss noticeably. The insertion loss can be improved to $0.7dB$ by this technique [35]. This method has been applied to the proposed system with the acceptable insertion loss of $0.8dB$.

2.4.3 Pulse Characterization Technique

To investigate the effects of various mechanisms on optical pulse in fiber, the pulse width is the main property which is examined. Hence, the pulse shape should be measured to extract this information. As the optical pulse time variation is much faster than that which can be measured by available electronic devices, the optical pulse cannot be measured directly. The pulse width is obtained by the auto-correlation measurement. Given function $I(t)$, the auto-correlation is defined as follows:

$$G(\tau) = \int I(t)I(t-\tau)dt \tag{2.11}$$

Pulse width can be acquired from $G(\tau)$. Table 2.1 represents the relationship between the pulse width of the auto-correlation function and the main function [36].

Table 2.1: Relationship between the main function and auto-correlation record

$I(t)$	$G(\tau)$	$\frac{\Delta\tau}{\Delta t}$
$sq(t)$	$(1-\lvert\tau\rvert) for \lvert\tau\rvert \leq 1, 0 otherwise$	1
$\exp(-2t^2)$	$\exp(-\tau^2)$	$\sqrt{2}$
$sech^2(t)$	$\frac{3(\tau\cosh(\tau)-\sinh(\tau))}{\sinh^3\tau}$	1.543

As the pulse width is the required parameter, the intensity auto-correlation is performed rather than linear auto-correlation which uses the electric field. The linear auto-correlation results in the inverse Fourier transform of the pulse spectrum which is not applicable for characterizing the pulse in this system. The measurement configuration for recording the intensity auto-correlation trace of the optical pulse is demonstrated in Fig. 2.8. The incident beam is divided into two beams using the beam splitter. The beams are reflected back by the mirrors afterwards; and finally, two beams arrive at the detector. If the distance of

the mirrors to the splitter is same, two pulses arrive at the same time. But, if one of the mirrors is mounted on a translational stage, the distance of the mirror to the splitter can be varied to realize a time delay between two received optical pulses.

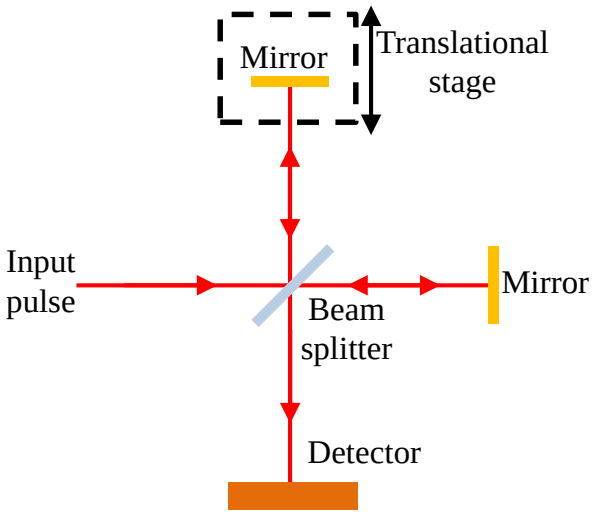

Figure 2.8: Auto-correlation measurement setup

To attain the intensity dependant auto-correlation, silicon detector is utilized for generation of the photocurrent at $1550nm$ wavelength. In fact, the main mechanism of the optical absorption in this silicon detector at $1550nm$ is two-photon absorption (TPA)[37]. As a consequence of intensity dependent absorption, the generated photo-current is proportional to the square of the optical pulse intensity. Therefore, the received signal for a particular time delay is obtained from Eq. 2.12 [36].

$$I_{photodetector}(\tau) = \int (intensity)^2 dt \tag{2.12}$$

$$
\begin{aligned}
(intensity)^2 &= |E(t) + E(t-\tau)|^4 \\
&= \left|\frac{1}{2} Re\left\{a(t)e^{j\omega_0 t} + a(t)e^{j\omega_0(t-\tau)}\right\}\right|^4 \\
&= 2|a(t)|^4 + 4|a(t)|^2|a(t-\tau)|^2 \\
&+ \{\{2(|a(t)|^2 + |a(t-\tau)|^2)a(t)a^*(t-\tau)e^{j\omega_0 t} + [a(t)a^*(t-\tau)]^2 e^{2j\omega_0 t}\} + c.c.\}
\end{aligned}
\tag{2.13}
$$

In Eq. 2.13 the first two terms result in a bias in the measured signal. The third term is exactly the intensity auto-correlation of the optical pulse. Therefore by changing the position of the mirror to realize various delays, the auto-correlation function can be obtained. As the duration of the optical pulse is in the range of 100fs, the movement of the stage should be in micro meter range to provide an acceptable accuracy. The rest of the terms in Eq. 2.13 are fast varying functions with ω_o frequency and eliminated by low pass filter of lock-in amplifier.

Employing TPA process brings two main advantages. First, this process can be provided in silicon detectors which are commercialized and available at a very low price. Moreover, this process can be used for very short optical pulses as it operates over a wide optical bandwidth [38]. However, the main problem is the low efficiency of this process as high power is required for acceptable measurement. This problem is resolved to some extent by employing an additional lens to tightly focus the optical beam on the detector.

2.4.4 Experimental Technique for Compression

A particular setup should be prepared to find the shortest optical pulse. In fact this short pulse can be obtained when the SFM and DCF fibers have right lengths respectively. As mentioned before, calculation of the exact value for these lengths is not very practical in the presence of the nonlinear effects; accordingly, a method should be introduced to figure out these values in a systematic way. To this end, as shown in Fig. 2.9, a setup is designed to receive the output pulse from the fiber and guide it to the auto-correlation setup. A bare fiber along with a lens which has short focal length are employed. In the subsequent step, the end part of the fiber is cut and cleaved to redo the pulse characterization once again. A shorter optical pulse is expected at each time. This procedure is performed repeatedly

until the optical pulse starts broadening.

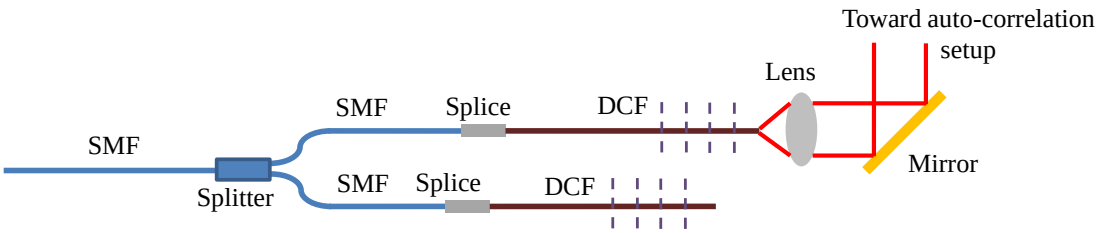

Figure 2.9: Measurement technique to find the right length for DCF

The characterization of the input optical pulse exhibits $100fs$ pulse width. Although this value is not the FWHM of the actual pulse, pulse width of the auto-correlation function can be used for comparison of the output pulse from the fiber and the initial pulse. Referring to Fig. 2.10, the auto-correlation records of the output pulse for four different fiber lengths are presented. The last result shows very good agreement with initial pulse width which means the effects can be compensated in an acceptable amount.

2.5 THz Measurement

2.5.1 Verification of Compressed Pulse

To verify the quality of the compressed pulses for generation of the THz signal, two measurements are performed and the results compared to each other: the generated THz signal from the initial free space pulse and the THz signal originating from the output pulse of the each fiber arm. To record the THz signal, same measurement setup is applied for both free space beam and output pulse of the fibers.

To measure THz signal, a free space beam measurement setup is utilized as shown in Fig. 2.1. The input optical pulse can either be the initial pulse or come from fiber end faces using a collimator. Since the configuration and measurement conditions are absolutely equivalent a fair comparison can be performed between THz signals. The measurement for the initial free space beam pulse is demonstrated in Fig. 2.11

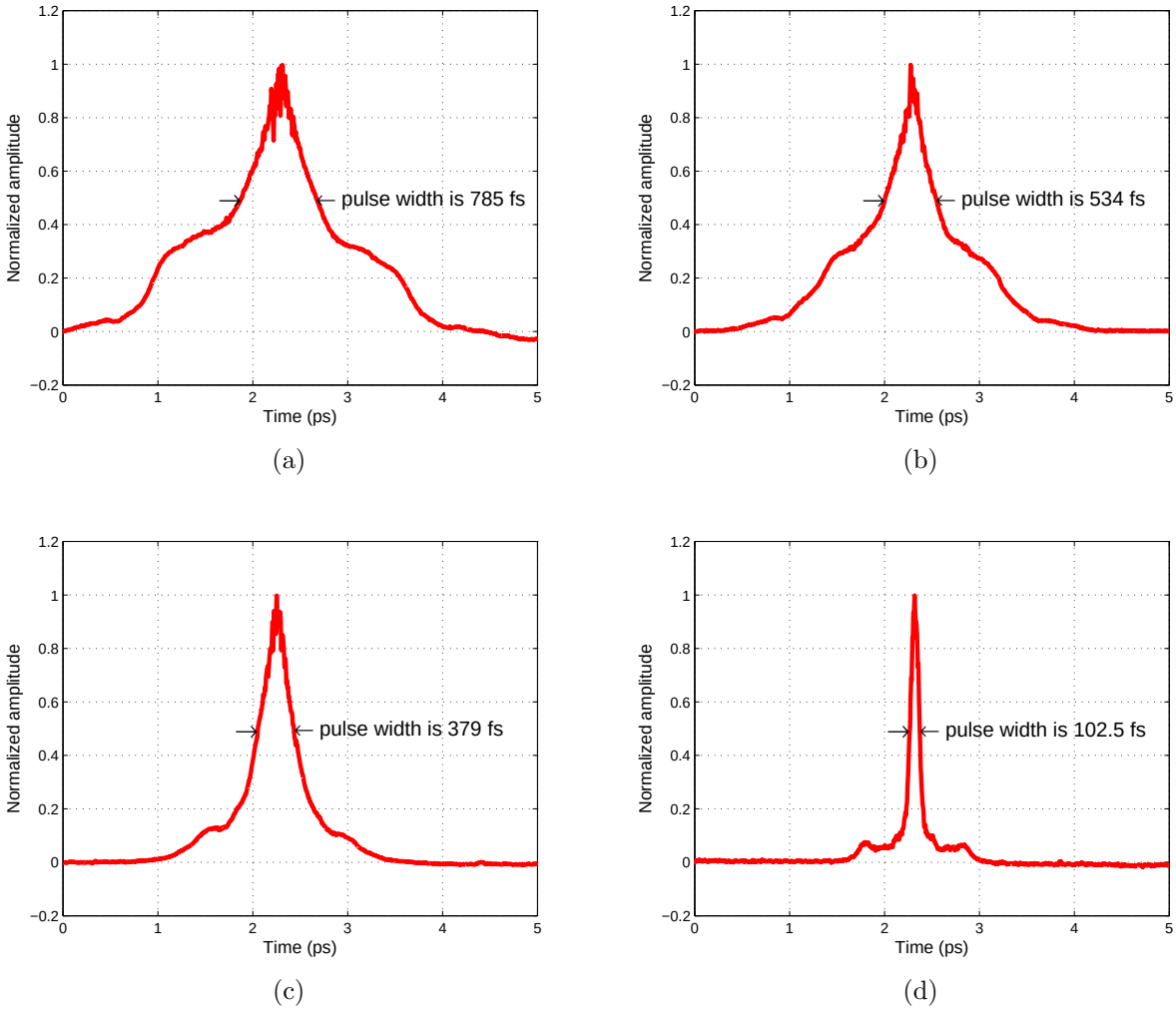

Figure 2.10: Autocorrelation record of the output pulse for four different DCF lengths: (a) Initial length (b) First cut (c) Second cut (d) Third cut

In the next step, the generated THz signal using the output pulse of the fibers is recorded. The measurement results are depicted in Fig. 2.12 for each arm. Considering the pulse width, the three measurement results are consistent and represent the same pulse width although a small variation in the shape of the THz pulse can be noticed. This variation originates from the propagation of the THz pulse in the system. In fact, As a consequence of particular alignment for each measurement, the detected pulse can be

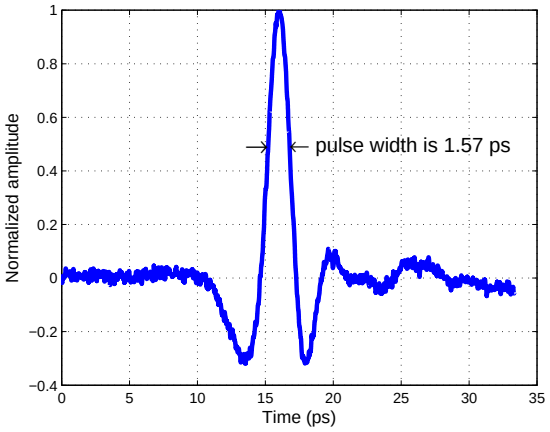

Figure 2.11: The Measurement results for the initial pulse using free beam space beam THz setup

affected. Furthermore, as the output power of each arm is not very high, the generated THz signal is slightly noisy.

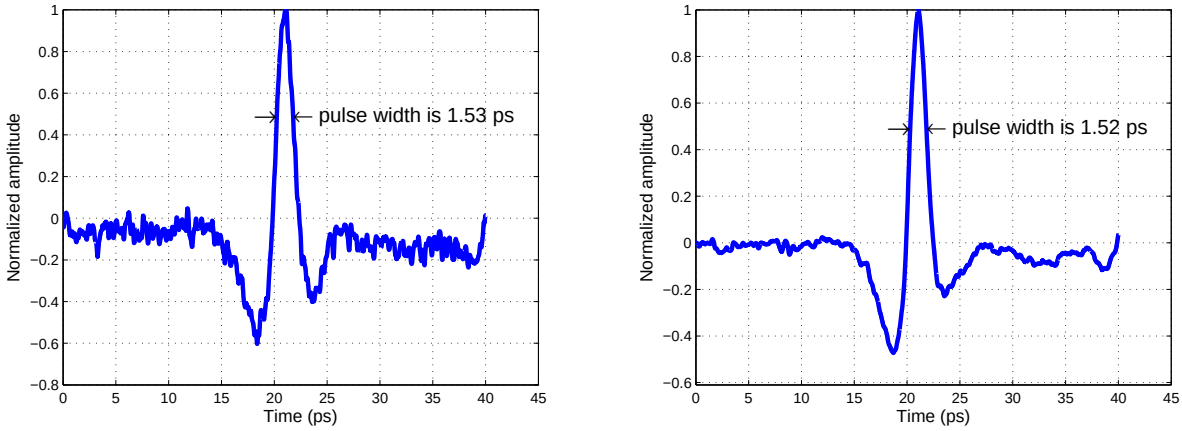

(a) (b)

Figure 2.12: The Measurement results for the output pulse of the fiber arms using free beam THz setup (a) First arm (b) Second arm

In this measurement, photoconductive antennas are used for transmitting and receiving the THz pulse. A large aperture structure is chosen for transmitter while the receiver is a

dipole antenna to enhance the received power. A special kind of material with high responsivity at $1.55\mu m$ wavelength is used as a nonlinear media for the generation of the THz signal. To strengthen the received signal, a silicon lens is mounted against the antenna to collect the THz signal power.

2.5.2 Fiber-Coupled Measurement

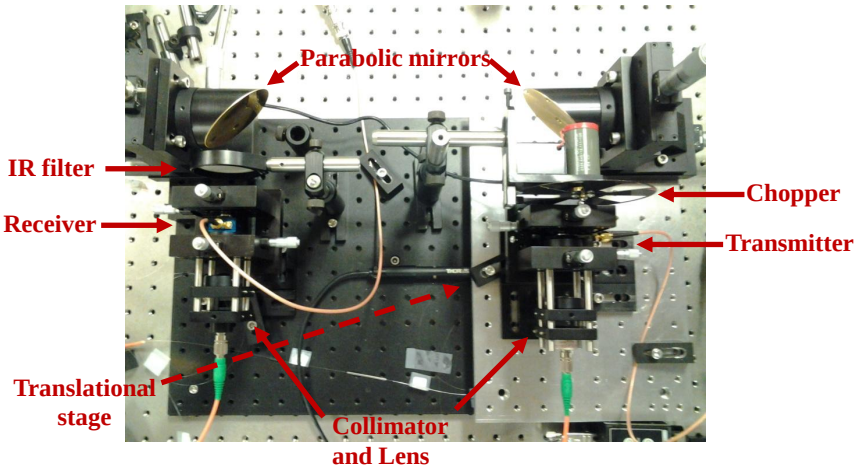

Figure 2.13: Picture of measurement setup for fiber-coupled THz Measurement

The final step is to conduct the THz measurements using the shorter fiber arm as the pump beam and the longer one as the probe beam. The measurement setup is demonstrated in Fig. 2.13. The output pulses of the fibers are focused on the photoconductive antennas through a collimator and a lens. The transmitter part is mounted on a translational stage to realize the time delay required for characterizing the THz pulse. The THz signal is guided toward the receiver antenna using gold coated off-axis parabolic mirrors. Furthermore, the IR filter which is transparent to THz signal is used to block part of the laser beam which is not absorbed in the photoconductive material and passes through the antenna. This IR beam can be detected in receiver and aggravates the SNR of the system. Although the THz signal is chopped in the current experiment, modulation of the signal can be performed by varying DC bias voltage of the transmitter.

The THz pulse is recorded using aforementioned setup and the result is represented in Fig. 2.14. The recorded pulse width is $1.32ps$ which is slightly shorter than the pulse

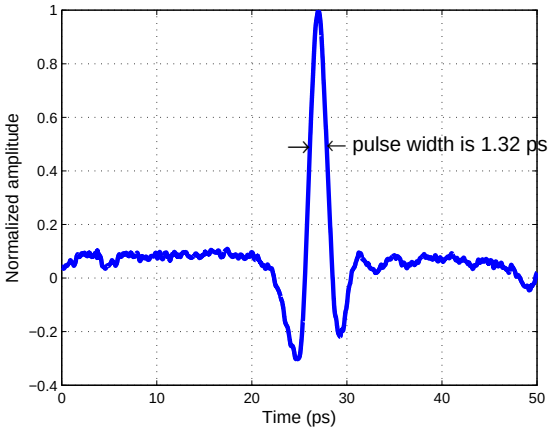

Figure 2.14: Fiber-coupled THz Measurement result

recorded in free space setup. The reason for this result is that the compensated pulses are a little shorter than the initial pulse. Therefore, this method can result in an even better THz pulses with broader spectrum for various applications.

Chapter 3

Source Integration

3.1 Introduction

THz systems can be developed for various applications in either free space configuration or guiding structures. Whereas most of the measurements in research laboratories are performed through a free space configuration, the other configurations based on THz guiding bring a number of advantages such as compactness and stability for different applications. Accordingly, integration of THz sources such as photomixers with THz waveguides is a crucial task to design an integrated THz structures for commercial applications. In THz spectroscopy systems which deploy guiding configuration, as a result of increasing the interaction length of the THz wave and the samples, the sensitivity of the system is enhanced substantially; consequently, the smaller amount of the sample can be used in THz measurement [39]. Some structures have been proposed to employ various THz waveguides such as metal wire [40], coplanar line [41], microstrip [42], and parallel plate waveguide [43] for guiding the THz wave in recent years for spectroscopy application. Although, those structures might be useful for some particular applications, they are either lossy in THz frequency or not suitable for realizing integrated systems. Although other types of waveguide with high efficiency such as dielectric waveguide is not broadband enough for time domain spectroscopy, they can be applied for frequency-domain THz spectroscopy [44].

Among the THz sources, the photonic based sources are generally more tunable and less costly as compared to the structures such as frequency multipliers. Another motivation is the advent of more compact tunable lasers source in the market with low price. In addition, they cover wide range of frequency while working at room temperature as opposed to the

Quantum cascade lasers, which need costly cryogenic cooler. Besides, these sources are suitable for packaging by employing photonic integrated circuit technology [45]. Owing to the aforementioned reasons, photnic-based Thz sources are the best option for integration with THz waveguide.

Furthermore, integration of THz source with a low loss waveguide brings the opportunity of developing a hybrid system as a transmitter for highly efficient imagers and ultra-broadband communication systems. In fact, due to high free space propagation loss in mm-wave and THz frequencies, Radio over Fiber (ROF) is the potential solution for extreme bandwidth communication over long distance. The essential component for these systems is an integrated photopic-based THz source to a transmitter to convert the optical signal to the THz signal. Some novel structures have been proposed through integration of the photometers chips to CPW line for photonic-based mm-wave and THz transmitters [46, 47] during the last decade.

In this chapter, a novel transition is proposed for integration of a photonic-based Thz source to a dielectric waveguide. In the first section, a brief background on THz dielectric waveguide and modeling the photomixer structure for the proposed transition are presented. Then the proposed structure and simulation results are discussed. Finally, the fabrication process is explained and the devices which are fabricated by micro-machining process are displayed.

3.2 Background

3.2.1 THz Dielectric Waveguide

A variety of the waveguides have been proposed for mm-wave and THz frequency range. Dielectric waveguides which usually have low propagation loss are more preferable for realizing highly efficient systems. In addition, a standard and low cost fabrication process can be developed for dielectric waveguide.

Depending on the operating frequency, various structures are employed for dielectric waveguide. At mm-wave and lower frequencies, the image line exhibits acceptable performance in terms of the propagation loss. The basic structure of the waveguide, as shown

in Fig. 3.1a, is the silicon slab over an infinite metallic plate. The dominant mode has the electric field in y direction (vertical to the ground plane). The main problem preventing this waveguide for operating at THz frequency is the conductor loss of the metallic plate as the conductor loss increase considerably due to the increase of the surface resistance.

A Silicon-on-Glass (SOG) dielectric waveguide, whose details are described in [48], is proposed for mm-wave hybrid integrated circuits. In the SOG dielectric waveguide, whose structure is shown in Fig. 3.1b, a silicon guiding channel is supported by a glass substrate. This structure can be considered as an alternative low-loss mm-wave waveguide. In the proposed dielectric waveguide, the dominant mode has a dominant transverse electric field component in x-direction, with an odd symmetry with respect to x (parallel to the glass slab). Additionally, through choosing appropriate dimensions for the dielectric slab, the dominant mode with the electric field in vertical direction and even symmetric field distribution is excited. The transverse electric field is more desirable as the electromagnetic fields spread less into the lossy glass structure and is more confined in silicon slab.

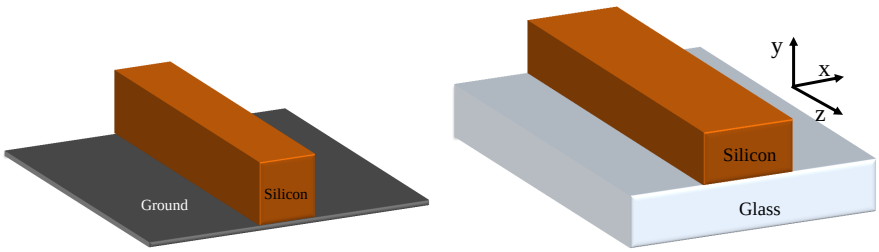

(a) (b)

Figure 3.1: Rectangular dielectric waveguide for mm-wave and THz frequency range: (a) Image line (b) Silicon-on-Glass (SOG)

Although the maximum operating frequency depends on the application, the glass substrate is quite lossy at THz frequencies upper than $200GHz$, as a result, some modifications are applied to the glass structure to reduce the dissipation of the dominant mode [48]. Replacing the glass slab with a grating glass structure is one feasible option which boosts the performance of the waveguide.

One problem with the dielectric waveguide is its gradual cut-off as compared to the sharp cut-off of closed metallic waveguides. Consequently, due to any kind of discontinuities, other modes can be excited and propagate through the waveguide. This effect is

alleviated by utilizing glass beneath the silicon to realize a single mode waveguide. In fact, higher order modes are more spread in glass structure and will be dissipated in this lossy media.

3.2.2 Photonic-Based THz Source

As explained in section 2.2, the basic structure for photonic-based THz source in both CW and pulse modes consists of a non-linear medium and a metallic structure to provide the dc bias as well as radiating the THz wave. In the design of the transition from photonic-based THz source to THz waveguide, the source can be modelled by a piece of dielectric with two metal strips on top of it as shown in Fig. 3.2. Additionally, the optical illumination and generation of the THz wave are not included in the simulation due to two reasons: first, including all the details in wave generation process makes simulations and optimization highly complex and time consuming; secondly, this part can be modeled by an lumped source as the size of the active region is much smaller than the THz wavelength in most of the cases.

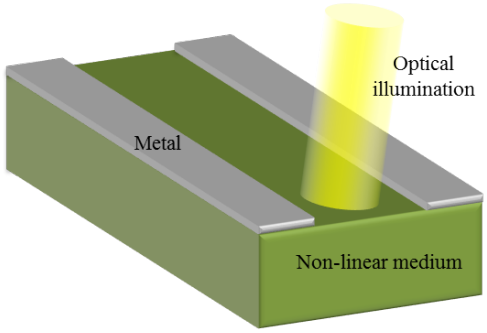

Figure 3.2: The model of the source structure which is considered for simulations

In the proposed structure, the metallic structure over the photonic source is in the form of a slot line for transmission of the THz wave over a very short distance to deliver THz energy to dielectric waveguide as will be explained later. The slot line itself can be considered as a waveguide for THz wave [49],[50] whereas the performance would not be acceptable due to surface roughness and finite conductivity of the metal at THz frequency. Additionally, the generated THz photocurrent due to optical illumination excites the dominant mode of the slot line as this THz current is in lateral direction; therefore, the excited

dominant mode in the slot line is used in the simulations. Therefore, the goal of this transition is to couple the dominant mode of the slot line to the THz waveguide. It should be noticed that the generated photo-current excites other modes in the slot line which degrades the optical to THz conversion efficiency. The efficiency can be improved through adding special design to the source structure to generate the photocurrent in such a way to excites only the dominant mode. However, this part is not discussed in the presented thesis.

The non-linear material in the source structure is GaAs which is quite lossy in THz frequency. The power absorption coefficient (α) has been obtained through time-domain spectroscopy of the crystalline high resistivity GaAs [51]. This calculation is based on the plane wave propagation in the GaAs. A fraction of the power dissipation originates from imaginary part of the permittivity and the rest comes from the conductivity of the GaAs. However, to simulate the structure under consideration, the material parameters of GaAs will be converted into suitable format for numerical solvers. To this end, the equivalent conductivity of the GaAs bulk structure is obtained by assuming that only GaAs conductivity contributes in loss mechanism. Therefore, the absorption coefficient can be converted to equivalent conductivity using Eq. 3.1 according to the plane wave equations.

$$\sigma = 2\alpha \frac{\sqrt{\omega^2 \epsilon \mu + \alpha^2}}{\omega \mu} \tag{3.1}$$

In Eq. 3.1, σ, α, ω, ϵ, and μ are denoting the conductivity, plane-wave absorption coefficient, frequency, the media permittivity and permeability, respectively. The conductivity versus frequency for GaAs is shown in Fig. 3.3. The high value of the conductivity can be highlighted through comparison with high resistivity silicon with conductivity less than $0.05 s/m$. Owing to the high GaAs absorption; the transition structure related to this part should be as short as possible to reduce the transition loss. As will be explained in the design procedure, the GaAs slab length is reduced by especial design for THz waveguide.

3.3 Method of Design

3.3.1 Proposed Configuration

As explained in section 3.2.1, the dielectric waveguide is employed for the integration of the THz source; therefore, the THz field coming from the slot line should be transformed

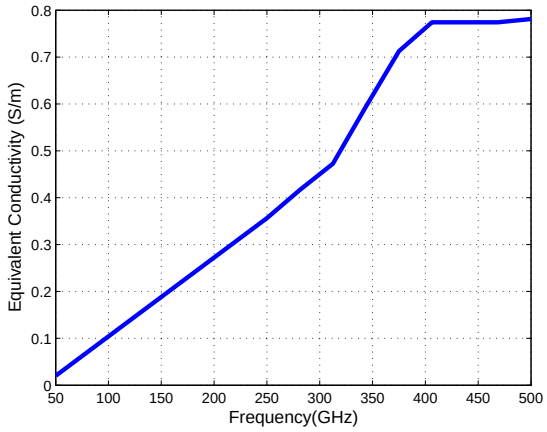

Figure 3.3: Equivalent conductivity over the operating frequency for GaAs

to the dominant mode of the SOG waveguide. A low loss transition is expected as both structures support a dominant mode with even symmertry. The basic idea for this transition is to flip source structure and mount it on the dielectric waveguide as represented in Fig. 3.4 . This kind of structure can introduce many benefits to the transition.

To minimize the transition loss a smooth structure without any sharp transitions is required. Hence, three tapered parts should be imagined: 1) where the electromagnetic waves come to the silicon slab, 2) at the end of the GaAs slab, 3) at the end of the slot line. These tapered parts can be in different orders although suitable order result in a good transmission coefficient.

In the proposed structure, the slot is tapered between the Si and GaAs slabs to enhance coupling. In fact, tapered slot line with free space on top can be used for antenna purpose and leads to huge radiation; as a consequence, this part is tapered between dielectric slabs to confine the energy in the structure. Furthermore, the mode field of the slot line is well-matched with the mode field of the two dielectric slabs on top of each other. To clarify, the maximum field of the slot line is between the metal strips; additionally, two dielectric slabs on top of each other support a dominant mode which confines field in the middle. Therefore, according to the proposed configuration, these two points are matched with each other and realizes maximum coupling. Consequently, the silicon slab should be tapered first, then the slot line, and finally the GaAs slab. Linear transition is utilized for dielectric slabs while a circular transition is applied for the slot line.

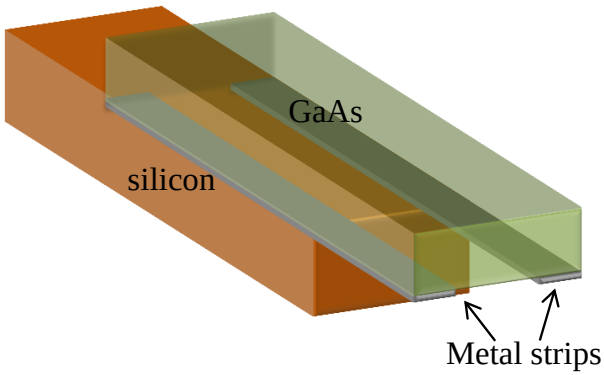

Figure 3.4: Primary source transition structure

3.3.2 Transition Length

Another consideration in the design is the length of the transition due to lossy source substrate. A simple way to decrease the length of the transition is to make the structure less sensitive to the length of the linear tapered part. Since the field is confined at the middle of the slot line and over its surface, the silicon waveguide is a huge discontinuity for incoming wave. To verify this fact, the field distribution at the lateral cross section of the slot line is demonstrated in Fig. 3.5a. To resolve this problem, a gap is applied between the two dielectric slabs to allow the THz energy comes between them without encountering to a significant discontinuity. Referring to Fig. 3.5b which represents side view of the structure, a step is made into the silicon waveguide to minimize the effect of tapering length for silicon and reduce the total length of the transition substantially.

For the particular dimensions, the effect of the gap depth on the transition loss is simulated and represented in Fig. 3.6. As expected by increasing the gap size, the transmission loss decreases noticeably. However, as a result of confinement of the electromagnetic field in a small region close to the surface, after some point, adding to the gap size has no effect on the results and even can degrade the transmission coefficient.

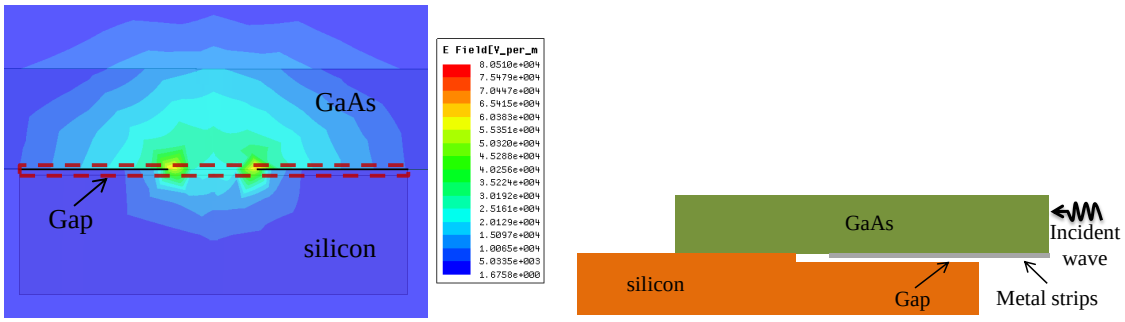

(a) (b)

Figure 3.5: (a) Field distribution of the slot line at the cross section (b) Side view of the structure to show the gap between the dielectric slabs

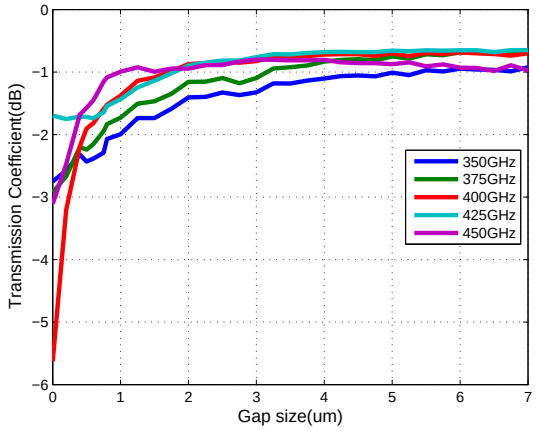

Figure 3.6: Transmission coefficient variation by changing the gap size between GaAs slab and DWG

3.4 Simulation Results

3.4.1 Optimization

Many parameters should be considered in optimization of the structure. Standard values corresponding to the operating frequency are chosen for the thickness of the silicon waveguide. Due to the some fabrication limitations, the GaAs slab should not be thicker than $100\mu m$. The width of the silicon waveguide is design to support the dominant mode with

acceptable propagation loss, and the GaAs width is close to the silicon width to improve coupling. The taper length is very short for the silicon waveguide while GaAs structure is tapered almost from the beginning of this slab to provide very smooth transition. The slot width and its tapered part are design to result in the best performance. Finally, the relative position of the GaAs structure and Si waveguide in longitudinal direction should be adjusted.

Fig. 3.7 represents the final design and the parameters for optimization. The dimensions for each frequency range are given in Table 5.1. The optimally designed structure has a good performance for various range of frequencies. As will be mentioned in section 3.5.1, due to some fabrication issues, a trapezoidal cross section is assumed for GaAs structure.

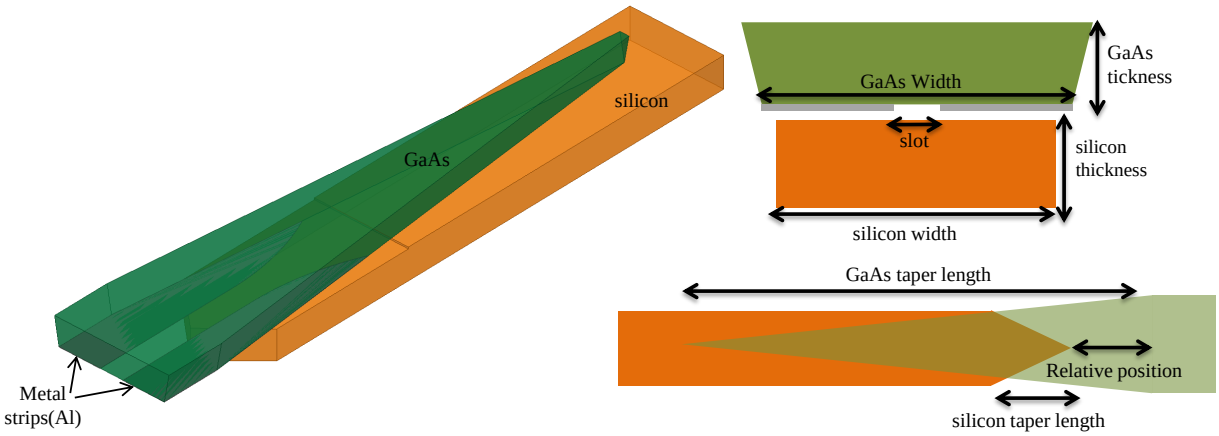

Figure 3.7: The transition structure at three different views and related parameters for optimization

3.4.2 Simulated Performance

The structure is simulated by HFSS and using parameters given in Table 5.1. The simulated results for reflection coefficient and transmission coefficient are depicted in Fig. 3.8. The transmission loss is better than $1dB$ over 25% bandwidth, and the reflection is better than $-20dB$ over the whole operating frequency range. The similar performance is obtained for other frequency ranges based on the dimensions in Table 5.1.

To investigate contribution of various processes in transition loss, simulations are repeated by removing one of the loss mechanism at each time. Based on the simulation

results, at the best point where transition loss is $0.6dB$, $0.3dB$ comes from GaAs loss, $0.2dB$ originates form finite conductivity of the metallic structure and $0.1dB$ is because of the transition itself. As expected, the high conductivity of GaAs has the main contribution to the total transition loss. This shows that GaAs is not appropriate for wave guiding at THz frequencies.

Table 3.1: Parameters value for rectangular profile at 100 GHz center frequency

Frequency range	285GHz-375GHz	350GHz-450GHz	390GHz-510GHz
GaAs thickness (μm)	95	90	80
GaAs width (μm)	460	380	330
GaAs taper length (μm)	2000	1750	1560
silicon thickness (μm)	100	100	100
silicon width (μm)	450	330	310
silicon taper length (μm)	280	150	130
slot (μm)	90	100	70
gap size (μm)	5	5	5
Relative position (μm)	340	300	265

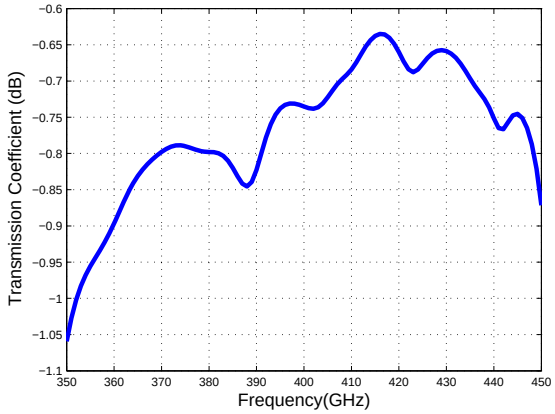

Figure 3.8: Transmition coefficient for THz source to dielectric waveguide transition

Moreover, the side view of the field distribution along the structure is represented in Fig. 3.9. At the beginning of the structure, most of the energy is concentrated over the surface

and inside the GaAs slab because of the slot line. After silicon tapered part, the field is more confined in the middle of the structure while it is distributed almost symmetrically in GaAs and silicon slabs due to the relatively similar permittivity of these two materials. Since the GaAs slab and slot line are tapered together the field gradually moves to silicon waveguide. Finally, the field is converted to the dominant mode of the waveguide at the end of the GaAs slab.

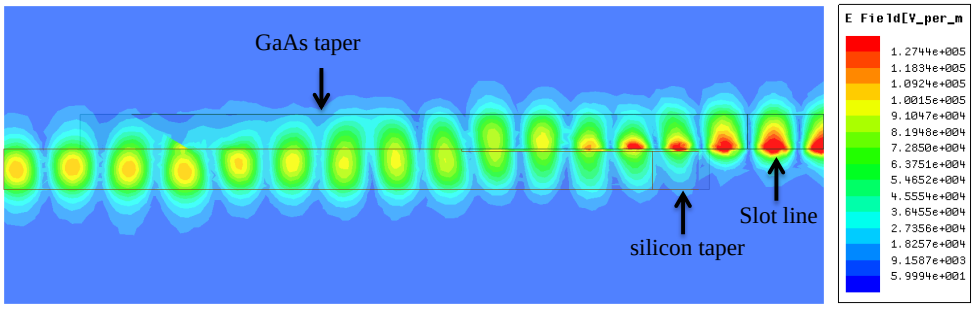

Figure 3.9: Field distribution over the longitudinal cross section

3.5 Fabrication

3.5.1 Process Steps

To facilitate measurement a back-to-back structure is fabricated. In the back-to-back configuration, the input energy is coupled to the DWG, then goes to the GaAs through the proposed transition and eventually comes back again to the dielectric waveguide. This structure can be measured using a network analyser with metallic waveguide ports. A linear tapered part is added to the ends of DWG as a transition to the metallic waveguide. This kind of measurement shows the transition loss of the structure without contribution of the optical process for generation of the THz signal. Additionally, to evaluate the performance of the system in an optical setup, still this configuration (back-to-back) can be utilized.

For this configuration, the source structure and silicon waveguide are fabricated separately; and in the next step, the GaAs structure is placed over the waveguide in symmetric manner. This alignment is feasible for lower frequency where the dimensions are large

enough; however, this task can be performed at higher frequencies using a nano-positioner.

The process developed by our group in recent years is applied for the fabrication of the silicon waveguide. Since the GaAs thickness is $100\mu m$, it should be bonded to a carrier wafer; consequently, the 2" double-side polished GaAs wafers are temporarily bonded to the polished side of 4" silicon substrate. The applied wax for bonding is a material with low thermal resistivity. It is also very thin to minimize its thermal resistivity. In addition, the melting point of the wax is more than 130^oC as the temperature might increase in various process. Then, GaAs wafers are ground to a thickness of $140 \pm 10\mu m$ and are polished to mirror polish without grinding marks using Chemical Mechanical Polishing/Planarization (CMP) tool. The final thickness is $100 \pm 10\mu m$ which is accurate enough for the structure.

The next step is to fabricate source structure which is dielectric slab with a patterned metal on top. To this end at least two masks are required one for GaAs structure and the other for metallic part. The steps are shown in Fig. 3.10, and the description for each step is as follows:

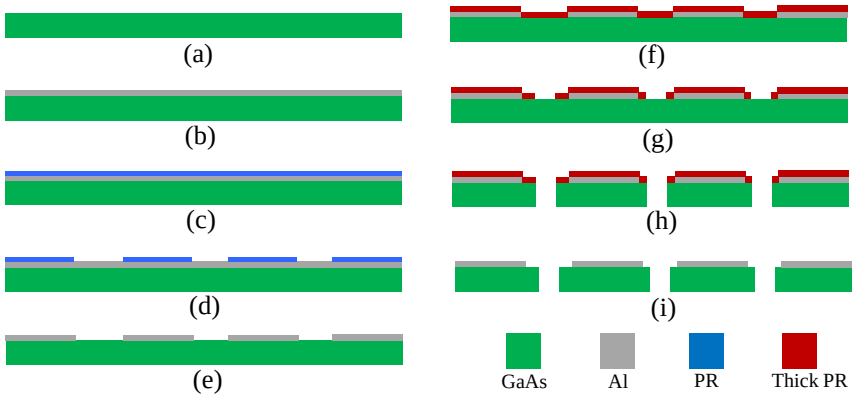

Figure 3.10: Fabrication steps for GaAs structures

(a) Cleaned GaAs wafer which is bonded to silicon wafer

(b) Doing multiple step Aluminum deposition by E-beam evaporation (1um thickness)

(c) Coating with thin photo-resist ($1.6\mu m$ thickness)

- Use Shipely 1811,Pour $5mL$

- Spread 10 seconds at $500RPM$
- Spin 60 seconds at $2000RPM$
- Soft baking by Use of the hotplate set to 115^oC for 90 seconds, Rehydrated for 15 minutes

(d) Lithography with the first mask (for metallic structure)

- The exposure time is 4.5 seconds (the lamp power is $25mw/cm^2$)
- developing the photo-resist using $MF-319$ for 90 seconds.

(e) Patterning the Aluminum

- Aluminum wet etchant for 15 minutes at room temperature. (special type of the etchant without nitric-acid should be used in order to prevent etching the GaAs)

(f) Coating with thick photo-resist ($11\mu m$)

- Use $AZP4620$, pour 5mL
- Spread 10 seconds at $500RPM$
- Spin 25 seconds at $2000RPM$
- Soft baking by Use of the hotplate set to 115^oC for 90 seconds, Rehydrated for 30 minutes.

(g) Lithography with the second mask (for GaAs structure)

- The exposure time is 29 seconds (the lamp power is $25mw/cm^2$)
- developing the photo-resist using $AZ400K$ for 120 seconds.

(h) GaAs dry etching

- Using Reactive Ion Etching (RIE) to etch through wafer

(i) Stripping the photo-resist mask

Using RIE for etching the GaAs impose two limitations. First the cross section is trapezoidal by 80^o degree angle instead of rectangular. Secondly, as well as low etch rate, the selectivity is $5-15:1$ for the thick photo-resist in this process; as a result, the thickness of the GaAs should be as low as possible. Based on the various attempts in laboratory, the GaAs thickness should be less than $100\mu m$.

3.5.2 Fabricated Devices

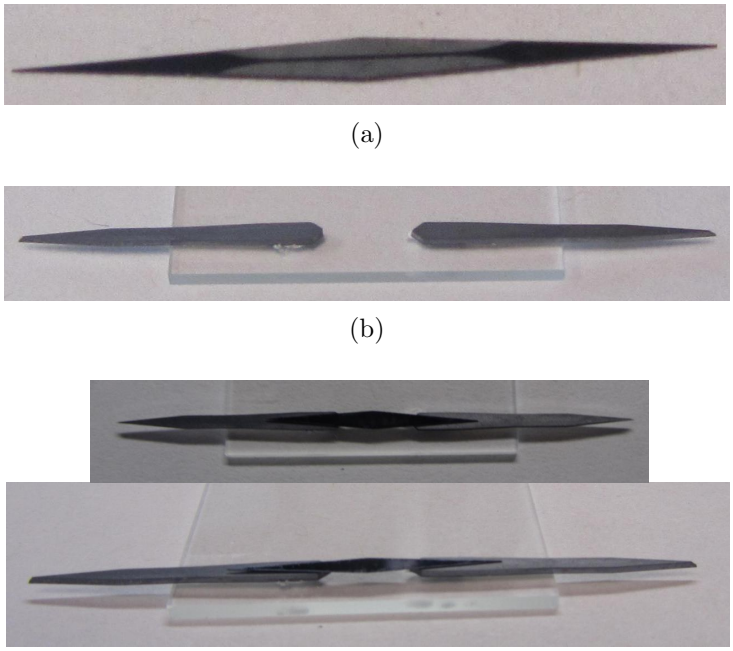

(a)

(b)

(c)

Figure 3.11: Fabricated structures: (a) Source structure (b) Dielectric waveguide part (c) The whole transition

The fabricated structures are demonstrated in Fig. 3.11. The first structure shows the GaAs part with the slot line. The next picture represent the back-to-back silicon waveguide. Two tapered parts are added to the DWG to provide a transition to metallic waveguide for testing. To improve the efficiency of this transition, no glass is used beneath the tapered part of DWG. In the last picture, the whole structure from two different views can be observed. Further alignment of the GaAs part over the silicon waveguide can be done when the measurement is performed to maximize the transmitted power.

Chapter 4

Active Device Integration

4.1 Introduction

Rapid progress in mm-wave and THz active device technologies has expanded the opportunity for low-cost compact integrated circuits and systems at mm-wave or even THz frequency range [52]. Owing to the high atmospheric losses at high frequency, transmitted or received signal should be amplified sufficiently; therefore, low-cost amplifiers should be employed close to the antenna front end for extreme bandwidth wireless communication at high frequency range [53]. Although on-chip circuits have been received considerable attention, it is not an effective solution for high performance millimeter-wave and THz circuits due to finite conductivity of the metallic structures and low resistivity of the chip substrate which lead to considerable loss in on-chip circuits. Therefore, on-chip passive circuits suffer from high insertion loss [54]. For instance, the measured efficiency of on-chip antennas have been less than 10 to 20 percent so far while the efficiency of the off-chip antennas at high frequencies have been enhanced enormously [55].

Hybrid integration can be considered as an alternative for mm-wave and THz circuits. In fact, the passive circuits can be implemented using a low-loss structures with the integrated active devices. In this chapter, a low-loss transition between an active device and the SOG waveguide is proposed and investigated. Two sections are dedicated for mm-wave and THz active devices, respectively. In fact, the different approaches for different frequency bands is employed to achieve the best performance.

4.2 Integration in MM-Wave Frequency Range

In this section, a low-loss transition between a mm-wave active device with planar metallic integrated circuit and a new Si-on-Glass (SOG) rectangular dielectric waveguide is designed. The detail of the SOG waveguide is explained in section 3.2.1. A well-known technique for this type of transition is flip-chip bonding, where the chip is mounted on the dielectric waveguide through flip-chip connection to a metallic circuit which is integrated with the waveguide [56]. In this work, the on-chip CPW port is directly connected to a CPW circuit attached to the dielectric waveguide using solder bumps which are deposited on the chip pads. The CPW circuit on the dielectric waveguide includes a transition mechanism which converts the CPW mode to the dielectric waveguide mode. Therefore, the transition from the CPW to the dielectric waveguide is an essential part in the integration of the active device with the dielectric waveguide. To the best of the of author's knowledge, it is the first time such transition at mm-wave is reported.

4.2.1 Proposed Structure

As shown in Fig. 4.1, the CPW can support two types of modes; the symmetric and the asymmetric ones. The symmetric mode, which is commonly used in the circuits, is the dominant mode of the CPW. Additionally, the SOG structure supports the two types of modes; however, for millimeter-wave frequencies where the power generation is costly and loss is a significant concern, the asymmetric mode is more preferable due to its low losses as explained in section 3.2.1. Since the preferable mode of the DWG is asymmetric, it weakly couples with the symmetric (dominant) mode of the CPW.

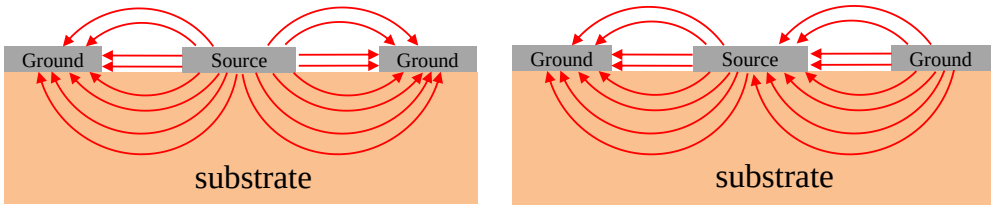

(a) (b)

Figure 4.1: Electric field at the cross section of the CPW line for the first two modes: (a) dominant (symmetrical) mode (b) second (asymmetrical) mode

Therefore, the DWG to CPW transition should convert the symmetric mode into the asymmetric one efficiently. The present section describes a conversion method based on the

introduction of 180^o phase shift between the two ground lines of the CPW. This phase shift at the beginning of the transition leads to a complete mode conversion (from asymmetric to symmetric) at the end of the transition. Based on this approach, the transition is considered as two separate parts: CPW to a slot line and the slot line to a dielectric waveguide.

Different structures have been proposed in literature for CPW to slot line transition. At low frequencies, providing open circuit at one of the ground lines and using the other line as the slot line is typical configuration in many designs [57, 58, 59], however these approaches are not applicable for higher frequency due to huge radiation loss. Since the field distribution of the dominant mode of slot line is close to the second mode of CPW, some efforts have been made to transfer the dominant mode to the second mode of CPW and couple the energy to slot line. Some of these structures, which shows good performance at higher frequencies, exploit a slow wave structure [60] or delay line [61] to compensate 180^o phase difference of ground lines. The structures in these methods are more frequency dependant and can decrease the operating bandwidth. Double stub transition [62] is applied to convert the second mode of CPW to the symmetrical CPW mode by adding 180^o phase shift. Two small stubs are more preferable than one long stub and can result in a better performance. Design of this transition in THz frequency is more challenging due to high metallic losses; however, these losses can be reduced by increasing the gap size in CPW line.

The asymmetry of the slot line dominant mode is similar to the DWG mode, but the maximum electric field in DWG mode is at the center of the waveguide while slot line concentrate the electric field at the top of the waveguide; therefore, the radiation loss of this part is due to the change in the confinement of the electric field from the top of the waveguide in the slot to the center of the DWG. Circular tapering is employed for this part to provide smooth and wavelength independent transition.

Apparently, direct connection of the two optimized structures (CPW to slot line and slot line to DWG) will not result in a good performance owing to the impedance mismatch of the slot lines and loading effect. To resolve this problem, a linear tapering part is added to the structure to match smoothly the first and the last part, respectively. Linear tapering is rather long although two other parts are realized in short length structures.

4.2.2 Method of Verification

Verification of the proposed transition is challenging. Since the primary tests and measurements are performed in passive mode without integration of the active devices, the most important task is to guarantee the coupling of the energy to the transition and evaluation of the transition itself. To this end, three different configurations are proposed for testing and shown in Fig. 4.2.

In the first configuration, the measurement should be done using network analyzer. A back-to back structure is designed in a way to start with the dielectric waveguide and end at the dielectric waveguide. Two linear tapered parts are added at the ends as the transition to metallic rectangular waveguide for the measurement. The results of this measurement cannot prove the performance as one can claim that the energy is not coupled to the transition and is guided only through the dielectric waveguide.

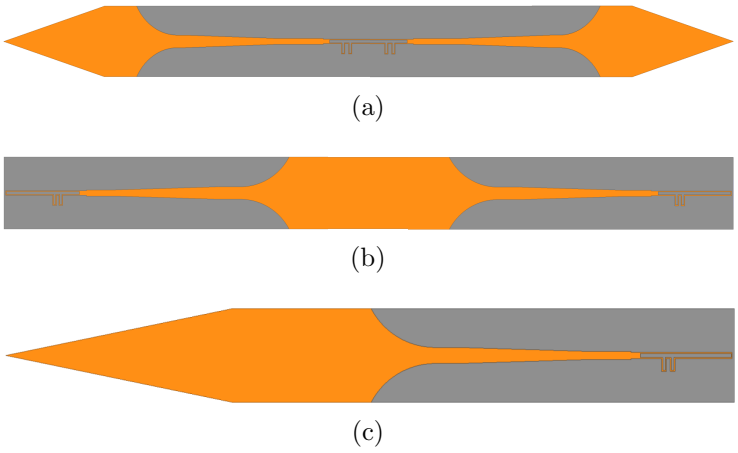

Figure 4.2: Top view of three different configurations for the verification of the transition (a) DWG back-to-back structure (b) CPW back-to-back structure (c) half structure

In the second configuration, the prober station should be employed for the measurement. A back-to back structure is designed in a way to start with the CPW line and end at the CPW line. No transition is required at the ends as the probes are connected directly to the line. Although this configuration ensures coupling the energy to the CPW line, one can claim that part of the received power comes from radiation. In fact those tapered slot structure can act as an antenna and transmit the power from one end to the other end.

In the last configuration, the combination of the network analyzer and prober station should be utilized to perform the measurement. To explain, a half structure is fabricated and a linear tapered part is added to the dielectric waveguide end. This configuration evaluates the real performance of the transition although the measurement would be more challenging.

4.2.3 Simulation and Optimization

To optimize the structure, the first part and the last part are optimized independently. The optimization parameters are represented in Fig. 4.3 which are source length, stubs width, distance between stubs, stub length, CPW width, CPW gap for the first part of the transition; and, slot width, radius of the circle for the last part of the transition. The optimization is done by genetic algorithm of HFSS due to so many parameters involving in the performance of the structure. The optimization goal is to minimize the insertion loss. The optimized values for 60GHz are mentioned in Table 4.1. This frequency has been chosen due to availability of the low-cost electronic devices although the structure can be easily redesigned for other frequencies.

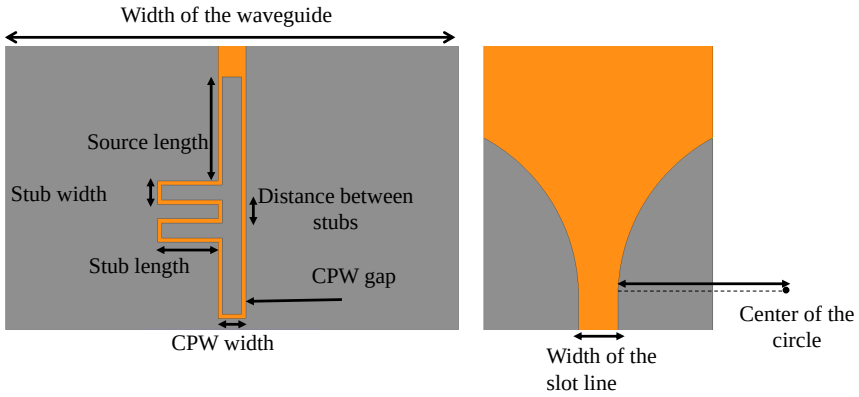

Figure 4.3: Transition parameters for optimization

Fig. 4.4 shows scattering parameters for three different configurations. The simulation results are obtained by HFSS at 60GHz. The slight variance in simulation results originates from difference in the basic structures. For instance, the tapered part has some effect in the first configuration, or the effects of the probe are included in the simulation for the

Table 4.1: Parameters value for optimized transition from CPW to DWG at 60 GHz center frequency

Frequency range	57GHz-63GHz
CPW width	88um
CPW gap	13um
Stub length	270um
Distance between stubs	65um
Stub width	68um
Source length	484um
Width of the waveguide	2mm
Center of the circle	1.6mm
Width of the slot line	362um

second configuration. The criterion for the bandwidth is reflection coefficient less than $-10dB$; therefore the transition works over the 10% of the center frequency. Furthermore, the minimal insertion loss is $1.7dB$ for the first two configurations and $0.9dB$ for the last configuration.

4.2.4 Fabrication

The designed structures are fabricated through standard recipes. The picture of three different fabricated structures are represented in Fig. 4.5. The tapered part for the first and the last structures are designed to couple the energy to rectangular waveguide for testing.

4.3 Integration in THz Frequency Range

The structure proposed in previous section is not appropriate for higher frequency although it can result in a very good performance at the lower frequencies where the proposed method in the current section cannot be applied. In fact, any kind of metallic connection such as flip-chip technique should be avoided due to the huge loss. However, in THz frequencies,

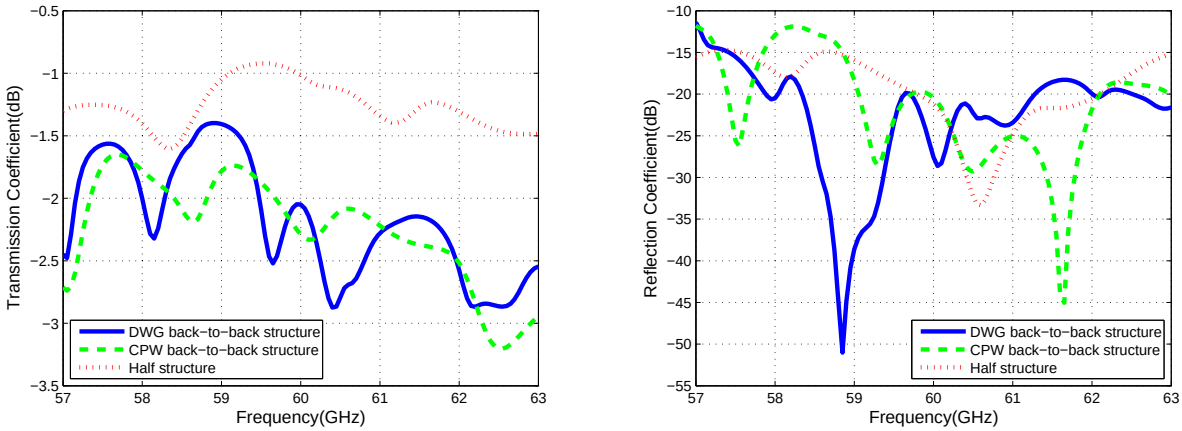

(a) (b)

Figure 4.4: Scattering parameters for three different configurations: (a) Transition coefficient (b) Reflection coefficient

because of very short wavelength, the transition structures are quite small. Therefore, the transition might be designed on the chip area to remove any metallic contact. To clarify, the incident energy of the waveguide can be absorbed by the active device through an on-chip antenna which acts as a coupling element. In addition to eliminating any metallic structures on the waveguide, the fabrication of this part would be easier and will be performed in fewer steps. This method cannot be applied at lower frequency as the chip area is extremely expensive and cannot be consumed for large transition design.

4.3.1 Proposed Structure

The chip structure is modeled by two parts: the substrate which is low resistivity silicon, and the top silicon dioxide layers used for metallic interconnect circuits and active device metalization. In passive/active metallic circuit layers, up to 10 metal layers are possible depending on the actual circuit design. In the proposed structure all of the metallic parts are removed except one for the antenna.

In the proposed structure, a dipole antenna is designed on the chip to couple the power from the chip to dielectric waveguide and vice versa. The dipole antenna is designed on

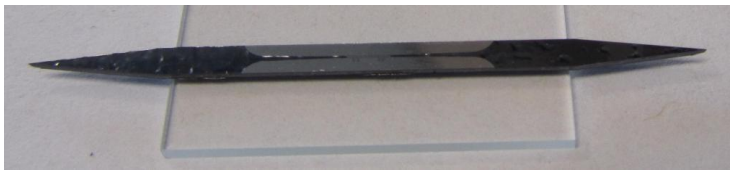

(a)

(b)

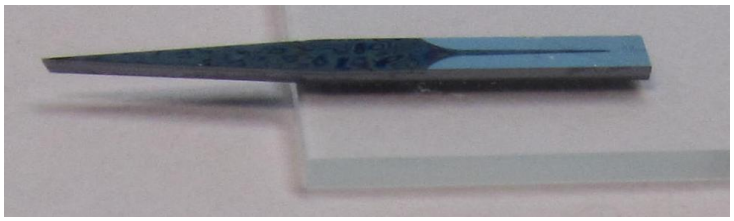

(c)

Figure 4.5: Fabricated structures for three different configurations (a) DWG back-to-back structure (b) CPW back-to-back structure (c) half structure

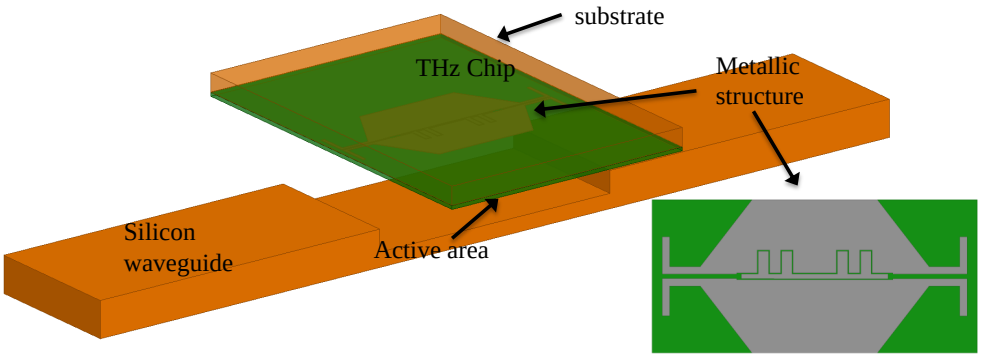

Figure 4.6: Proposed structure for active device integration at THz frequencies

coplanar line; as a consequence, a CPW to coplanar line transition is introduced to the structure. The idea for this transition, similar to the previous section, is to deploy two stubs to realize 180^o phase shift. The direction of the dipole antenna is matched with the polarization of DWG dominant mode.

The position of the dipole antenna is crucial for achieving the maximal coupling. To this end, a section of the dielectric waveguide will be etched to create a recessed region, where the faced-down chip will be placed. Herein, the dipole antenna is positioned in the middle of the waveguide where the field is strong. The exploded view of the proposed structure is presented in Fig. 4.6 where the chip is removed from its final position to show the details of the transition.

4.3.2 Simulation Results

The structure is simulated using HFSS. The substrate loss is included in the simulation as it affects the performance of the transition significantly. The resistivity of the substrate is quite low and is considered $50 ohm.cm$. The simulated generalized scattering matrix versus frequency is represented in Fig. 4.7. The return loss is quite low over a wide range of frequencies. The transition operates over 25% bandwidth. The insertion loss, mainly due to the lossy substrate, is acceptable at this range of frequency. The performance can be improved by $1dB$ if high-resistivity silicon is used for the chip substrate as some companies have started to market this kind of high resistivity substrate chip.

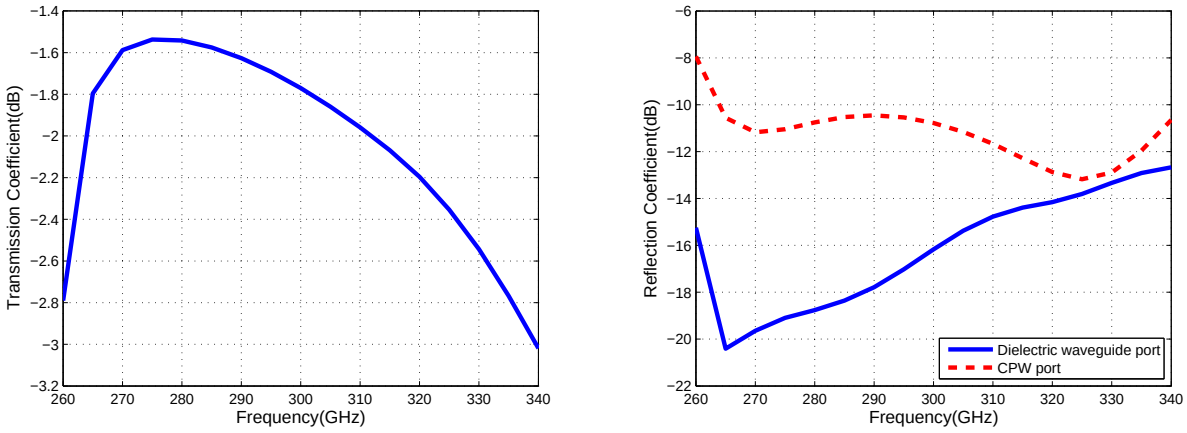

(a) (b)

Figure 4.7: Generalized scattering parameters for half structure (CPW to dielectric waveguide) (a) Transmission coefficient (b) Reflection coefficient

Chapter 5

Dielectric Antenna

5.1 Introduction

High data rate communication and sensing applications including High Definition Video Streaming, wireless back-haul links and high resolution imaging and radar have caused huge interest and numerous research and development efforts in millimetre-wave (mm-Wave) device, antenna, and packaging technologies. However, wireless mm-Wave systems are still quite complex and costly mainly because of the complexity of packaging and antenna technologies. Significant parasitics as well as the increased power lost in both the system components and the space propagation at this range of frequencies are among major challenges which device/system developers in this range of frequencies are constantly dealing with. High efficiency is a crucial design requirement for mm-Wave components and packaging technologies.

The efficiency and the gain of the antenna are the key factors in mm-Wave front-end performance. To achieve high gain and high radiation efficiency, a new low-loss grating antenna concept is proposed here. In general, fully-dielectric travelling wave antennas [63, 64] satisfy the aforementioned requirements. Unlike low frequencies, mm-Wave travelling wave antennas are compact and hence are more desirable for practical applications. In addition to their highly directive beam and efficient radiation, no complicated feeding network is required for travelling wave antennas as opposed to the conventional antenna arrays architecture.

The frequency scanning based upon the variation of the main beam direction versus frequency, is one of the interesting properties of grating antennas which have been widely used in mm-Wave Radar and Imaging systems [65]. This idea provides a low cost and a simple way for beam steering in the absence of any beam forming network.

Different approaches have been employed for realizing frequency scanning. Some new designs for enhancing the efficiency of the printed leaky wave antennas[66] (a slow wave structure modulated by periodic discontinuities) and frequency scanning [67] have been proposed recently. Furthermore, new structures using engineered material with negative permittivity and permeability have received attentions in the recent years[68]. The electromagnetic properties provide some new features such as the broad side radiation. Finally, some non-planar designs for frequency scanning have also been reported [69, 70]. However, planar structures are essential for achieving integrated mmWave system for the emerging high speed applications.

In the current chapter, two important considerations have been taken into account for the antenna design. First, the antenna structure should have the minimal amount of losses to achieve high efficiency. To this end, a fully dielectric structure should be considered. Although, the radiation efficiency in some metallic structures is remarkably improved using dielectric resonator antennas, the fabrication complexity at higher frequency is still a significant challenge in practical realization of such structures. [71]. Dielectric grating structure has been introduced as a leaky wave antenna [72]. A top-grating fully-dielectric antenna has been investigated recently [73]. The structures with various grating profiles have been fabricated and verified. But in higher frequency, due to the fabrication costs and difficulties, top grating antenna is not easy to realize and the grating profile is uncontrollable. Therefore, the second consideration is to reduce the fabrication cost and complexity of the antenna structure to make it practical for commercial systems.

Among the proposed technologies for the mmWave high efficiency antennas is the high resistivity silicon based antenna systems [74], [75]. Silicon is the most popular material for micro-machining and particularly the high resistivity substrates (un-doped) have offered high performance in mmWave [76]. This chapter proposes a new all-Silicon one-dimensional periodic leaky-wave antenna optimized for frequency scanning applications at mm-wave.

Next section provides details on the proposed structure along with its design strategy. The performance optimization process is discussed afterward. The last section presents

the measurement setup and the experimental results.

5.2 Proposed Structure

In the proposed antenna, shown in Fig. 5.1, radiation is realized through applying grating on the sides of the structure. In higher frequency, due to the fabrication constraints,only rectangular grating profile is feasible on top of the dielectric waveguide. Therefore, to eliminate this limitation and apply benefits of the various grating profiles, side grating structure can be considered as an alternative approach for dielectric grating antenna. Although the proposed concept can be applied to a wide range of grating shapes, without loss of generality, only rectangular and triangular grating profiles are investigated in this chapter. The 3D view of the proposed rectangular grating antenna and the top view of one unit cell are illustrated in Fig. 5.1.

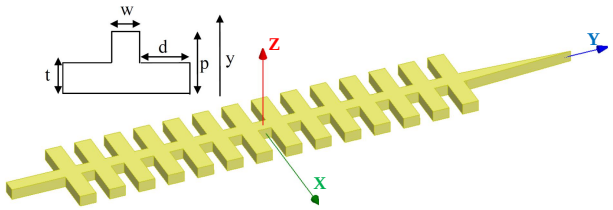

Figure 5.1: 3D view of rectangular side grating antenna and the top view of one unit cell

The proposed structure consists of an image dielectric waveguide with corrugations on its both sides. The whole structure lies on an infinite conductor sheet (ground plane). The un-corrugated image waveguide is designed such that single-mode operation is achieved. In this case, the dominant mode is TM_0 to the y direction (referring to Fig. 5.1). The tapered part, at the end of the antenna, radiates remaining power to the free space to prevent reflected power which leads to creating another lobe in the reverse direction. Therefore, if the antenna has a sufficiently long length, the end tapered section can be removed since negligible amount of the power reaches the end of antenna.

Deep understanding of the radiation mechanism of the structure is crucial for the antenna design and finding the initial values of the antenna dimensions for design optimiza-

tion. Floquet's mode expansion of electric field around the antenna is given by [63]:

$$E(x,y,z) = \sum_{n=-\infty}^{n=\infty} a_n(x,z)e^{-j\beta_n y - \alpha_n y}, \beta_n = \beta_0 + \frac{2n\pi}{p} \tag{5.1}$$

In Eq. 5.1, β_n represents propagation constant of order n space harmonic and α_n is the leakage constant of the propagating mode number "n". As a matter of fact that only fast waves radiate, typically, radiation is due to the $n = -1$ space harmonic. However, in some structure the zeroth order space harmonic can also be a fast wave [67]. It should be mentioned that the antenna should be designed to suppress the radiation from $n = -2$ space harmonic which leads to strong side lobes in radiation pattern.In addition, the direction of the main beam of the nth space harmonic is given by:

$$\theta = \sin^{-1}(\frac{\beta_n}{k_0}) = \sin^{-1}(\frac{\beta_0 + 2n\pi/p}{k_0}) \tag{5.2}$$

where k_0 is the wave number in free space. This equation is helpful in finding the initial design values for antenna optimization. Frequency scanning is achieved by changing frequency, which in turn varies the free space propagation constant and the beam direction respectively.

In the proposed antenna, $n = 0$ space harmonic is a non radiating slow wave. The dispersion diagram for the first mode over the operating bandwidth is obtained using two different commercial softwares, HFSS and COMSOL, and represented in Fig. 5.3. As expected, the results are close to each other. One unit cell of the rectangular grating antenna with optimized dimensions is simulated in eigenmode solver of the two aforementioned softwares with periodic boundary condition over the end planes; therefore, Fig. 5.3 shows dispersion diagram for an infinite structure.

If the radiation is due to the $n = -1$ space harmonic, the main beam direction can be found from Eq. 5.2 when $n = -1$. To obtain the beam direction, the value of the β_0 in Eq. 5.1 can be approximated by propagation constant of the image line without grating. The image line propagation constant can be obtained using 2D mode analysis of COMSOL. The field distribution at the cross section of the image line as well as the dispersion diagram is demonstrated in Fig. 5.2.

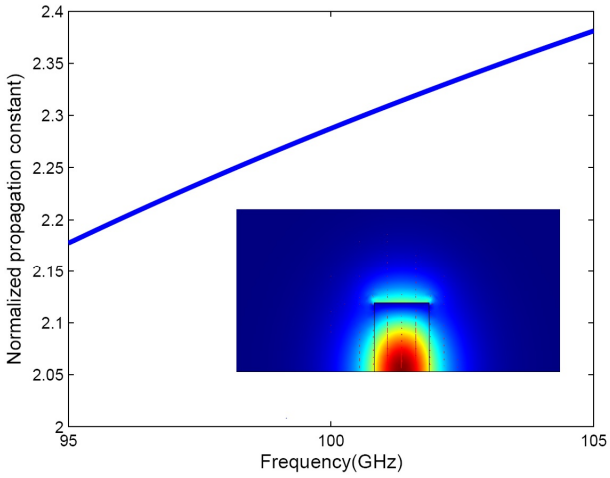

Figure 5.2: Normailized propagation constant of the image line. Inset shows the field distribution at the cross section of the image line obtained by COMSOL.

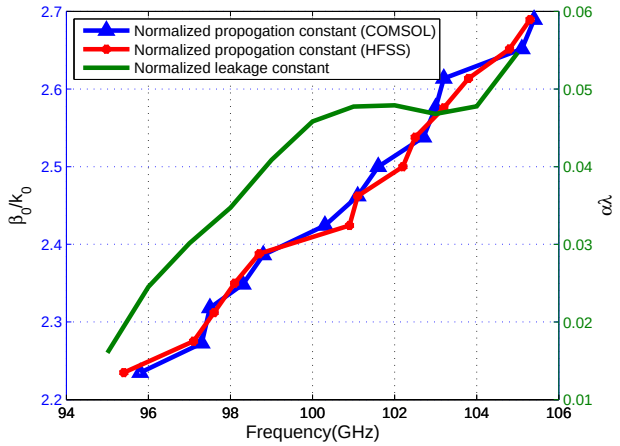

Figure 5.3: Normalized dispersion diagram of the periodic structure using COMSOL and HFSS. Also, normalized leakage constant of the antenna

The beam directions obtained from the aforementioned approximate method, numerical analysis of the infinite periodic structure using HFSS and COMSOL, HFSS simulation of the finite structure with the grating, and measured data respectively, are compared in Fig. 5.4. It is to mention that the beam directions from approximate method and infinite periodic structure are obtained by substituting β_0 in Eq. 5.2 . The agreement between these three plots related to infinite structure and the one resulted from full-wave simulation

of the finite length structure confirms that first, the radiation comes from $n = -1$ space harmonics, and secondly, the dispersion diagram of the image line can be used for initial approximation of the main beam direction. Although good agreement between the infinite and the finite structure simulation results can be observed, the small difference is owing to the fact that the radiation of the reflected wave from the finite length antenna end to the free space leads to a small change in the main beam direction.

Leakage constant should be determined in such a way that antenna radiates all the power; therefore, longer antenna requires lower leakage constant and vice versa. To find the leakage constant, antenna structure can be simulated with two ports. The normalized leakage constant is found by approximating the decaying power along the antenna by an exponential function. The normalized leakage constant obtained by this method presented in Fig. 5.3. An interesting behaviour can be observed in the frequency range from 100GHz to 102GHz where the normalized leakage constant is frequency independent.

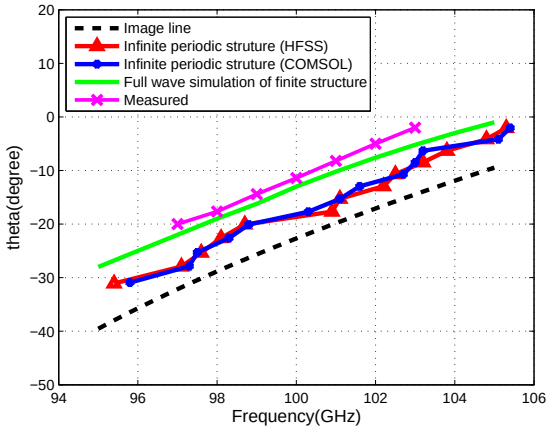

Figure 5.4: Main beam angle vs frequency.

Since the structure is almost lossless, the leakage constant (α) is directly related to radiation efficiency. The radiation efficiency of the antenna is defined as the ratio of the total radiated power through the grating structure to the input power. Therefore, the radiation efficiency can be expressed as follows:

$$\eta = 1 - \|S_{11}\|^2 - \|S_{21}\|^2 \tag{5.3}$$

Where η is the radiation efficiency; and, S_{21} is obtained by two ports simulation of the antenna. Although, high radiation efficiency can be realized in lossless antennas but this

parameter also depends on the aperture efficiency of the antenna. High leakage constant leads to very poor aperture efficiency. In the proposed antenna the radiation efficiency is higher than 90% over the entire bandwidth.

5.3 Design Optimization

The optimization variables for proposed rectangular grating antenna are the period of the grating, axial ratio, image line width, and grating depth, which are denoted by $p, a(t/p), w$ and d respectively (see Fig. 5.1). To achieve the maximal leakage constant, axial ratio should be close to 0.5 [73, 77]. The upper limit for the period of the structure can be obtained based on the fact that single beam scanning over the entire range is desirable. Therefore, the radiation should only arise from the $n = -1$ space harmonics while other harmonics (especially $n = -2$) remain non-radiating slow waves. To satisfy this condition, β_{-2} should be less than k_0. In addition, the initial value of the period of the structure is determined roughly by direction of the main beam at central frequency using the dispersion diagram of the image line and Eq. 5.2.

The grating length should be chosen to provide a uniform power leakage along the antenna. Efficient use of antenna aperture is the main key to achieve a high gain antenna. Grating length should be as large as possible to increase the antenna aperture and consequently antenna gain. However, too long grating length leads to a huge discontinuities, non-uniform power radiation and lower aperture efficiency. For finding the optimum length, parametric simulation on this variable can be performed.

Furthermore, the thickness of the silicon waveguide typically is given. It is assumed $0.4mm$ in this structure. The width of the silicon should be close to the thickness to support more efficiently the dominant TM mode. In table 5.1, the designed and optimized values are compared.

Table 5.1: Parameters value for the grating profile

Antenna Parameters	p	a	w	d
Designed (mm)	1.14	0.5	0.4	–
optimized (mm)	1.10	0.55	0.5	1.30

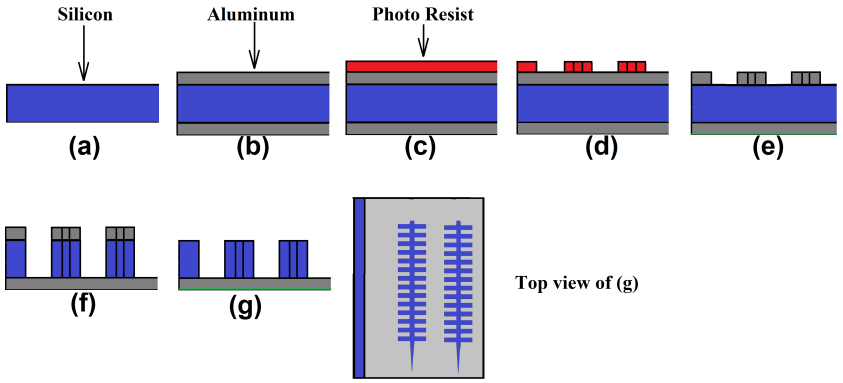

Figure 5.5: Single print through wafer silicon etching process for the antenna fabrication.

5.4 Fabrication

A Single-Mask process is used for the fabrication. Standard steps and recipes are used to achieve both low cost and reproducibility. Our substrate wafer is high resistivity silicon [1 0 0] with a relative permittivity (ϵ_r) of 11.9, a resistivity (ρ) of $3.2K\Omega cm$, with a thickness of $400\mu m \pm 10\mu m$.

The process steps can be summarized as shown in Fig. 5.5. In this figure, the cross section of the structure is shown. Simply, we (a) clean our high resistivity silicon wafer in piranha solution before we (b) sputter $0.5\mu m$ of Aluminum at each side of the silicon substrate. Then, we (c) coat it with thin photo resist (Shipely 1811 with a thickness of $\sim 1.3\mu m$) on one side of the Aluminum before performing (d) optical lithography with the 5 inch mask. The Aluminum is then (e) patterned using wet etching process. The back side Aluminum is protected with tape. After that, (f) Deep reactive-ion-etching (DRIE)[78](Standard Bosch process) is done for the thickness t (a carrier wafer is used during the through wafer etching). DRIE gives right angle profile for through wafer etching. Then we (g) strip the Aluminum mask with wet etching and do dicing to extract the antenna. The fabricated antenna along with the test fixture are shown in Fig. 5.6.

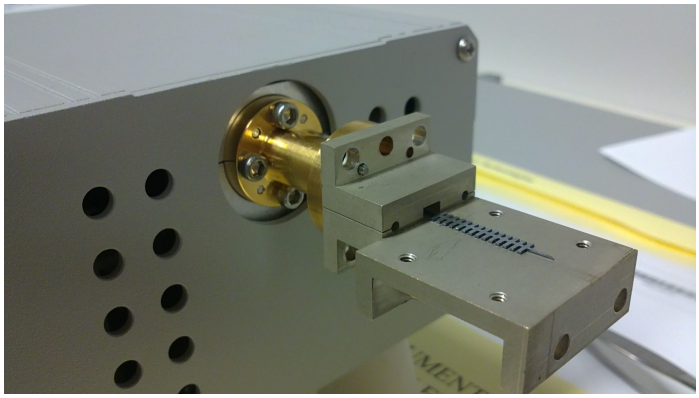

Figure 5.6: Picture of the rectangular side grating antenna mounted on the test fixture

5.5 Results

The corrugations in the proposed structure can be implemented in any two dimensional profiles. In this section, the performance of the triangular profile is compared with rectangular profile. The top view of two different profiles are shown in Fig. 5.7. Some specific behaviours are expected for each type of profiles.
Similar procedure can be followed for triangular grating to find the initial values for antenna optimization. The axial ratio is one to exploit the whole part of unit cell for radiation. Whereas, the radiation in rectangular grating antenna is due to the discontinuities in the unit cells, the whole part of unit cell is radiating in triangular grating antenna. This unique feature of triangular grating brings some remarkable advantages for this kind of profile.
To asses with the advantage of the proposed side grating concept, we will present the results in a comparison fashion.

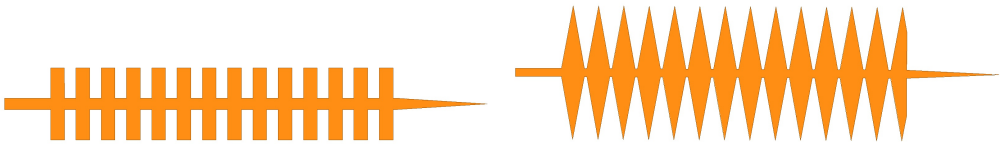

Figure 5.7: Top view of side grating antenna with two different profiles: (a) rectangular and (b) triangular

5.5.1 Bandwidth and Gain

The triangular profile can be considered as an extension of the rectangular profile, a set of rectangular part with different grating lengths which are placed on side of each other. Therefore, the antenna with triangular profile should result in a wider bandwidth since the operating frequency of the antenna depends on the grating length. To define the bandwidth of the antenna, reflection coefficient and maximal gain of the antenna is taken into account. The antenna gain is represented in Fig. 5.8 for both rectangular and triangular profile. Additionally, comparison of the simulated and measured return loss is demonstrated in Fig. 5.9 and Fig. 5.10 for both types of grating. Good agreement is obtained between simulated and measured results. Our figure of merit for definition of the bandwidth is reflection coefficient less than $-10dB$ and $1.5dB$ variation in maximal gain. Hence, the operating frequency range for rectangular grating antenna is from $97GHz$ to $104GHz$ ($\approx 7\%$); whereas, triangular grating antenna works over wide frequency band, from $84GHz$ to $102GHz$ ($\approx 19\%$)

Moreover, based on the results obtained by HFSS the maximal gain for rectangular and triangular grating are close to $17dB$. This value is obtained for a particular antenna length ($15mm \approx 5\lambda_0$), however, antenna gain can be enhanced by increasing the antenna length and reducing the leakage constant.

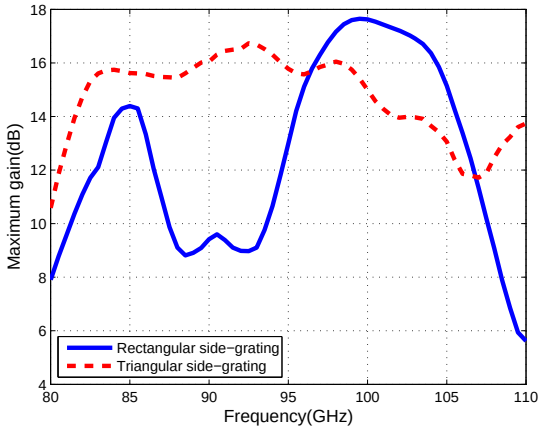

Figure 5.8: Maximum gain of rectangular and triangular profiles

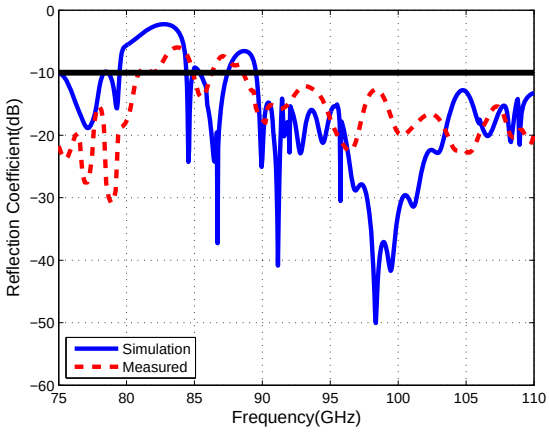

Figure 5.9: Return loss over the w-band frequency range for rectangular side-grating

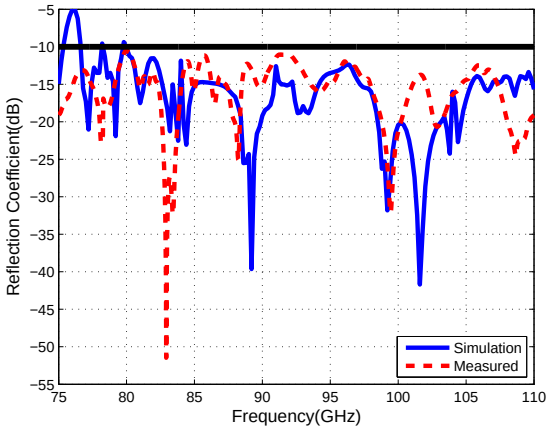

Figure 5.10: Return loss over the w-band frequency range for triangular side-grating

5.5.2 Broadside Radiation

One major issue in dielectric grating antennas is the broad side radiation when $\beta_0 d$ is equal to 2π. To explain, as the beam goes toward the broadside, the attenuation constant and the gain of antenna degrades, and the main part of the power reflects back to the source. In fact, at the open stop-band point, the reflected powers from unit cells add constructively. The same situation happens when $\beta_0 d = \pi$, but the fast wave doesn't exist in that region to radiate. For the planar periodic antenna, open stop-band effect is mitigated in some

novel designs by increasing the radiating elements in the unit cells [79] or using a composite right/lefthanded (CRLH) structures [80].

To investigate open stop-band effect in the proposed structures, the maximal gain of antenna, as a good indication of this phenomena, has been considered. Referring to Fig. 5.8, the gain of antenna drops dramatically at the particular frequency corresponding to the broad side radiation. However, to achieve broadside radiation, open stop-band effect is reduced enormously in the triangular grating. As the beam direction becomes closer to the broadside the gain of antenna drops by around 1dB at 96GHz which is acceptable based on our criteria for the bandwidth.

The measured main beam direction is compared with simulated results in Fig. 5.4 and Fig. 5.11 for rectangular and triangular grating, respectively. 20 degree and 35 degree frequency scanning are observed with a good agreement with simulated results for rectangular and triangular profile, respectively .

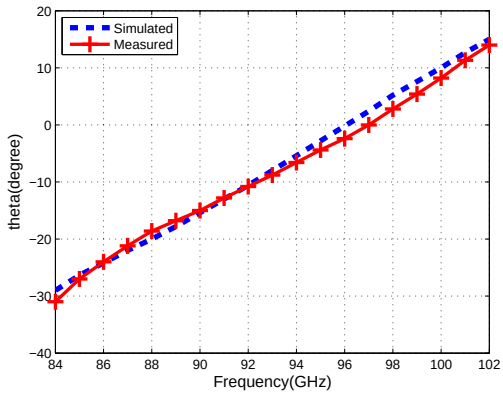

Figure 5.11: Comparison of the simulated and the measured frequency scanning for triangular side-grating antenna

5.5.3 Radiation Pattern

The far-field of the antenna is calculated using measured near-field. Some parameters such as scan window and distance from probe to the antenna are critical in the near-field mea-

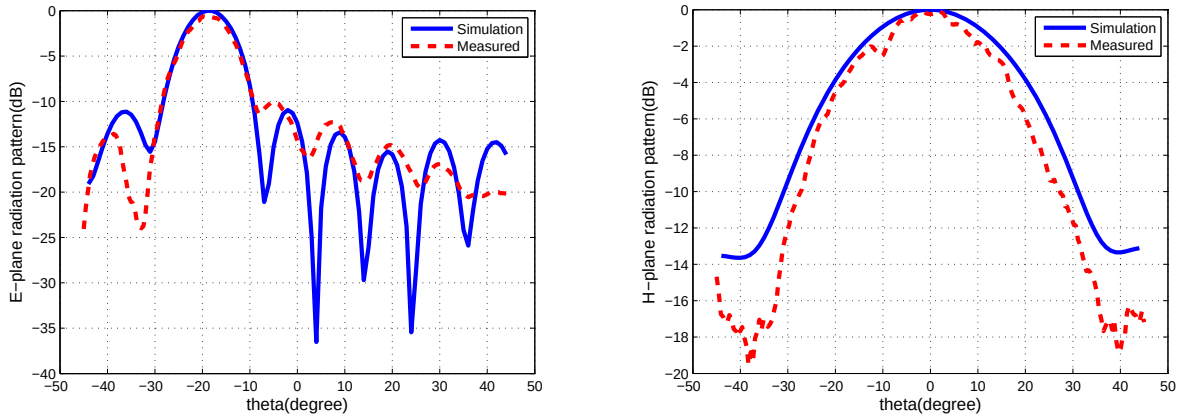

(a) (b)

Figure 5.12: Comparison of the simulated and measured radiation pattern for rectangular side-grating antenna: (a) E-plane (b) H-plane

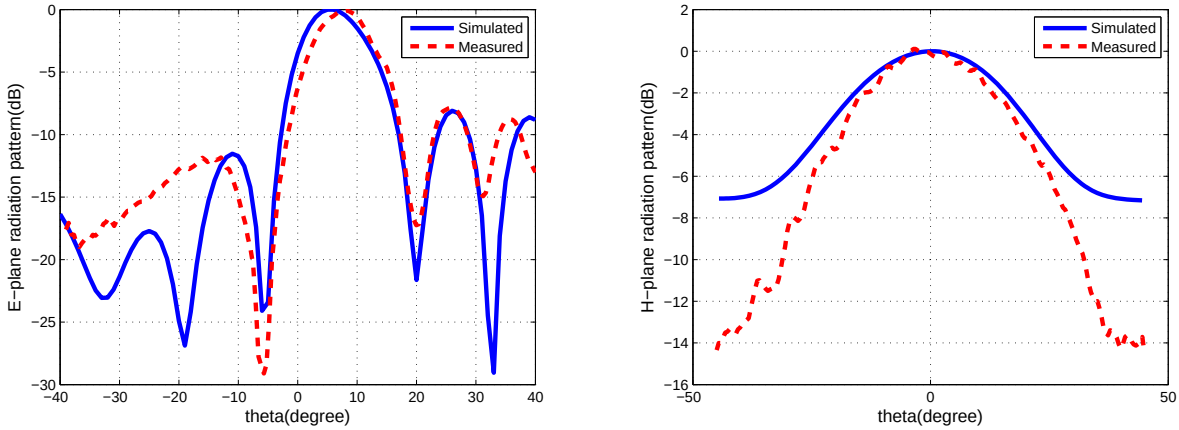

(a) (b)

Figure 5.13: Comparison of the simulated and measured radiation pattern for triangular side-grating antenna: (a) E-plane (b) H-plane

surement. For instance, the scan window size should be large enough to have very weak field at the edges of the window. In addition, the probe should be as close as possible to enhance the signal to noise ratio(SNR) while introducing the minimum near field interac-

tion with antenna.

The antenna far field has linear polarization in theta direction (referring to Fig. 5.1); therefore, yz plane is the principal E-plane. The E-plane and H-plane radiation pattern at $98GHz$ is represented in Fig. 5.12 and Fig. 5.13 for rectangular and triangular grating, respectively. Since the antenna is along y direction the beam width is narrower in E-plane. Furthermore, the side lob level is improved in triangular grating.

Chapter 6

Summery and Future Research

6.1 Summery

In the research reported here, different components and integration technologies for realizing a compact, robust and low cost THz system were investigated and novel structure were proposed. In the second chapter the feasibility of developing all-fiber system for optical beam delivery was presented. The theory of the pulse propagation through the fiber was reviewed and numerical result showed how nonlinearity affects the optical pulse. THz measurements were conducted to verify the performance of the developed system.

Coupling of the generated THz signal in the photomixer structure to the dielectric waveguide through a novel transition with low insertion loss was presented in chapter 3. The simulation results demonstrated insertion loss as low as $1dB$ over 25% bandwidth up to 650GHz. The challenges in fabrication process were described and fabricated structures were represented. This transition can be applied in many application such as communication and imaging to provide a low cost, tunable and integrated THz source.

Chapter 4 focused on the integration of the active devices such as mm-wave and THz amplifiers to the dielectric waveguide. Rapid progress in electronics devices and demand for enhancing the power budget of THz systems are main motivation for developing this transition. Novel transitions were proposed for mm-wave and THz frequency with very low insertion loss. The transitions were fabricated for 60GHz through a standard process.

Finally, chapter 5 proposed a new high efficiency side-grating antenna for frequency scanning applications. This type of grating simplified the fabrication process and introduced flexibility in the grating profile. Various profiles were investigated for the grating structure. The proposed antenna achieved an efficiency of 90% and a gain of $18dB$. The measurements showed a good agreement with the simulation results. A simple and low cost fabrication process for the proposed antenna was also presented.

6.2 Future Research

It should be noted that the presented structures and configurations for realizing a THz system are just for proof of concept and many other issues are required to be addressed. Consequently, the main line of research in the future can be to combine different structures and analyze system level integration issues in a more comprehensive manner. Furthermore, each section individually should be completed and improved. The future works can be classified as follows:

- The fiber coupled THz measurement should be performed using better materials and antenna structure to reach to the better bandwidth at $1.55\mu m$ pumping wavelength.
- To verify the simulation results, an appropriate measurement setup should be design for the source integration structure to perform optical measurement as well as using network analyzer.
- A technique for characterization of the high frequency structure for active device integration should be devised.
- Other alternative approaches for dielectric antenna structure should be studied, designed, fabricated and measured as a comparison to the side-grating antenna.
- The proposed component technologies should be optimized and combined for development of a particular complete system such as a sub-mmW/THz imager or sensor. System level measurement should be performed to verify the performance of the whole system.

References

[1] B.M. Fischer, H. Helm, and P.U. Jepsen. Chemical recognition with broadband thz spectroscopy. *Proceedings of the IEEE*, 95(8):1592 –1604, aug. 2007.

[2] Zhanke Yan, Yibin Ying, Hongjian Zhang, and Haiyan Yu. Research progress of terahertz wave technology in food inspection. pages 63730R–63730R–10, 2006.

[3] Kaori Fukunaga, Yuichi Ogawa, Shin'ichiro Hayashi, and Iwao Hosako. Application of terahertz spectroscopy for character recognition in a medieval manuscript. *IEICE Electronics Express*, 5(7):223–228, 2008.

[4] N. Vieweg, N. Krumbholz, T. Hasek, R. Wilk, V. Bartels, C. Keseberg, V. Pethukhov, M. Mikulics, L. Wetenkamp, and M. Koch. Fiber-coupled thz spectroscopy for monitoring polymeric compounding processes. pages 66163M–66163M–8, 2007.

[5] Hai-Bo Liu, Hua Zhong, N. Karpowicz, Yunqing Chen, and Xi-Cheng Zhang. Terahertz spectroscopy and imaging for defense and security applications. *Proceedings of the IEEE*, 95(8):1514 –1527, aug. 2007.

[6] Ho-Jin Song and T. Nagatsuma. Present and future of terahertz communications. *Terahertz Science and Technology, IEEE Transactions on*, 1(1):256 –263, sept. 2011.

[7] John Federici and Lothar Moeller. Review of terahertz and subterahertz wireless communications. *Journal of Applied Physics*, 107(11):111101, 2010.

[8] L.-P. Schmidt, S. Biber, G. Rehm, and K. Huber. Thz measurement technologies and applications. In *Microwaves, Radar and Wireless Communications, 2002. MIKON-2002. 14th International Conference on*, volume 2, pages 581 – 587 vol.2, 2002.

[9] G. Chattopadhyay. Technology, capabilities, and performance of low power terahertz sources. *Terahertz Science and Technology, IEEE Transactions on*, 1(1):33 –53, sept. 2011.

[10] Sushil Kumar, Qing Hu, and John L. Reno. 186 k operation of terahertz quantum-cascade lasers based on a diagonal design. *Applied Physics Letters*, 94(13):131105, 2009.

[11] Benjamin Williams, Sushil Kumar, Qing Hu, and John Reno. Operation of terahertz quantum-cascade lasers at 164 k in pulsed mode and at 117 k in continuous-wave mode. *Opt. Express*, 13(9):3331–3339, May 2005.

[12] A. Wade, G. Fedorov, D. Smirnov, S. Kumar, BS Williams, Q. Hu, and JL Reno. Magnetic-field-assisted terahertz quantum cascade laser operating up to 225 k. *Nature Photonics*, 3(1):41–45, 2008.

[13] D. Saeedkia and S. Safavi-Naeini. Terahertz photonics: Optoelectronic techniques for generation and detection of terahertz waves. *Lightwave Technology, Journal of*, 26(15):2409 –2423, aug.1, 2008.

[14] L.A. Samoska. An overview of solid-state integrated circuit amplifiers in the submillimeter-wave and thz regime. *Terahertz Science and Technology, IEEE Transactions on*, 1(1):9 –24, sept. 2011.

[15] Nan-Wei Chen, Hsuan-Ju Tsai, Fon-Ming Kuo, and Jin-Wei Shi. High-speed -band integrated photonic transmitter for radio-over-fiber applications. *Microwave Theory and Techniques, IEEE Transactions on*, 59(4):978 –986, april 2011.

[16] B. Sartorius, H. Roehle, H. Künzel, J. Böttcher, M. Schlak, D. Stanze, H. Venghaus, and M. Schell. All-fiber terahertz time-domain spectrometer operating at 1.5 μm telecom wavelengths. *Opt. Express*, 16(13):9565–9570, Jun 2008.

[17] Frank Ellrich, Tristan Weinland, Daniel Molter, Joachim Jonuscheit, and Rene Beigang. Compact fiber-coupled terahertz spectroscopy system pumped at 800 nm wavelength. *Review of Scientific Instruments*, 82(5):053102, 2011.

[18] S. A. Crooker. Fiber-coupled antennas for ultrafast coherent terahertz spectroscopy in low temperatures and high magnetic fields. *Review of Scientific Instruments*, 73(9):3258–3264, 2002.

[19] Young Bin Ji, Eui Su Lee, Sang-Hoon Kim, Joo-Hiuk Son, and Tae-In Jeon. A miniaturized fiber-coupled terahertz endoscope system. *Opt. Express*, 17(19):17082–17087, Sep 2009.

[20] R. Inoue, Y. Ohno, and M. Tonouchi. Development of fiber-coupled compact terahertz time-domain spectroscopy imaging head. *Jpn. J. Appl. Phys*, 45:7928–7932, 2006.

[21] S. Verghese, K.A. McIntosh, and E.R. Brown. Highly tunable fiber-coupled photomixers with coherent terahertz output power. *Microwave Theory and Techniques, IEEE Transactions on*, 45(8):1301 –1309, aug 1997.

[22] S. L. Dexheimer. *Ultrafast Optics*. Boca Raton : CRC Press, 2008.

[23] B.R. Brown. Thz generation by photomixing in ultrafast photoconductors. *International Journal of High Speed Electronics and Systems*, 13(2):497, 2003.

[24] G. P. Agrawa. *Nonlinear Fiber Optics*. U.K.: Academic, 2nd edition, 1995.

[25] G. P. Agrawa. *Contemporary Nonlinear Optics*. Academic Press, San Diego, CA, 1992.

[26] Thiab R Taha and Mark I Ablowitz. Analytical and numerical aspects of certain nonlinear evolution equations. ii. numerical, nonlinear schrdinger equation. *Journal of Computational Physics*, 55(2):203 – 230, 1984.

[27] E. Treacy. Optical pulse compression with diffraction gratings. *Quantum Electronics, IEEE Journal of*, 5(9):454 – 458, sep 1969.

[28] Francois Salin and Alain Brun. Dispersion compensation for femtosecond pulses using high-index prisms. *Journal of Applied Physics*, 61(10):4736–4739, 1987.

[29] J. Heppner and J. Kuhl. Intracavity chirp compensation in a colliding pulse modelocked laser using thin-film interferometers. *Applied Physics Letters*, 47(5):453–455, 1985.

[30] Mankei Tsang, Demetri Psaltis, and Fiorenzo G. Omenetto. Reverse propagation of femtosecond pulses in optical fibers. *Opt. Lett.*, 28(20):1873–1875, Oct 2003.

[31] Mankei Tsang and Demetri Psaltis. Dispersion and nonlinearity compensation by spectral phase conjugation. *Opt. Lett.*, 28(17):1558–1560, Sep 2003.

[32] Fiorenzo G. Omenetto, Antoinette J. Taylor, Mark D. Moores, and David H. Reitze. Adaptive control of femtosecond pulse propagation in optical fibers. *Opt. Lett.*, 26(12):938–940, Jun 2001.

[33] A. D. Yablonr. *Optical Fiber Fusion Splicing*. Springer, 2005.

[34] B. Edvold and L. Gruner-Nielsen. New technique for reducing the splice loss to dispersion compensating fiber. In *Optical Communication, 1996. ECOC '96. 22nd European Conference on*, volume 2, pages 245 –248 vol.2, sept. 1996.

[35] Lars Grner-Nielsen, Stig Nissen Knudsen, Bent Edvold, Torben Veng, Dorte Magnussen, C.Christian Larsen, and Hans Damsgaard. Dispersion compensating fibers. *Optical Fiber Technology*, 6(2):164 – 180, 2000.

[36] A. M. Weiner. *Ultrafast Optics*. John Wiley and Sons, Hoboken, New Jersey, 2009.

[37] T. K. Liang, H. K. Tsang, I. E. Day, J. Drake, A. P. Knights, and M. Asghari. Silicon waveguide two-photon absorption detector at 1.5 mu m wavelength for autocorrelation measurements. *Applied Physics Letters*, 81(7):1323–1325, 2002.

[38] Jinendra K. Ranka, Alexander L. Gaeta, Andrius Baltuska, Maxim S. Pshenichnikov, and Douwe A. Wiersma. Autocorrelation measurement of 6-fs pulses based on the two-photon-induced photocurrent in a gaasp photodiode. *Opt. Lett.*, 22(17):1344–1346, Sep 1997.

[39] G. Gallot, S. P. Jamison, R. W. McGowan, and D. Grischkowsky. Terahertz waveguides. *J. Opt. Soc. Am. B*, 17(5):851–863, May 2000.

[40] Markus Walther, Mark R. Freeman, and Frank A. Hegmann. Metal-wire terahertz time-domain spectroscopy. *Applied Physics Letters*, 87(26):261107, 2005.

[41] R. Sprik, I. N. Duling III, C.-C. Chi, and D. Grischkowsky. Far infrared spectroscopy with subpicosecond electrical pulses on transmission lines. *Applied Physics Letters*, 51(7):548–550, 1987.

[42] M. B. Byrne, J. Cunningham, K. Tych, A. D. Burnett, M. R. Stringer, C. D. Wood, L. Dazhang, M. Lachab, E. H. Linfield, and A. G. Davies. Terahertz vibrational absorption spectroscopy using microstrip-line waveguides. *Applied Physics Letters*, 93(18):182904, 2008.

[43] Joseph S. Melinger, S. Sree Harsha, N. Laman, and D. Grischkowsky. Guided-wave terahertz spectroscopy of molecular solids (invited). *J. Opt. Soc. Am. B*, 26(9):A79–A89, Sep 2009.

[44] G. Mouret, S. Matton, R. Bocquet, F. Hindle, E. Peytavit, J.F. Lampin, and D. Lippens. Far-infrared cw difference-frequency generation using vertically integrated and planar low temperature grown gaas photomixers: application to h_2s rotational

spectrum up to 3 thz. *Applied Physics B: Lasers and Optics*, 79:725–729, 2004. 10.1007/s00340-004-1607-2.

[45] L. Ponnampalam, R.J. Steed, M.J. Fice, C.C. Renaud, D.C. Rogers, D.G. Moodie, G.D. Maxwell, I.F. Lealman, M.J. Robertson, L. Pavlovic, L. Naglic, M. Vidmar, and A.J. Seeds. A compact tunable coherent terahertz source based on an hybrid integrated optical phase-lock loop. In *Microwave Photonics (MWP), 2010 IEEE Topical Meeting on*, pages 151 –154, oct. 2010.

[46] Nan-Wei Chen, Jin-Wei Shi, Hsuan-Ju Tsai, Jhih-Min Wun, Fong-Ming Kuo, Jeffery Hesler, Thomas W. Crowe, and John E. Bowers. Design and demonstration of ultra-fast w-band photonic transmitter-mixer and detectors for 25 gbits/sec error-free wireless linking. *Opt. Express*, 20(19):21223–21234, Sep 2012.

[47] A. Sto andhr, S. Babiel, P.J. Cannard, B. Charbonnier, F. van Dijk, S. Fedderwitz, D. Moodie, L. Pavlovic, L. Ponnampalam, C.C. Renaud, D. Rogers, V. Rymanov, A. Seeds, A.G. Steffan, A. Umbach, and M. Weiss. Millimeter-wave photonic components for broadband wireless systems. *Microwave Theory and Techniques, IEEE Transactions on*, 58(11):3071 –3082, nov. 2010.

[48] N. Ranjkesh, M. Basha, and S. Safavi-Naeini. Silicon-on-glass dielectric waveguide for thz integrated system. 2012 (to be submitted).

[49] Shinji Yanagi, Masayuki Onuma, Jiro Kitagawa, and Yutaka Kadoya. Propagation of terahertz pulses on coplanar strip-lines on low permittivity substrates and a spectroscopy application. *Applied Physics Express*, 1(1):012009–012009–3, 2008.

[50] S. Gupta, J.F. Whitaker, and G.A. Mourou. Subpicosecond pulse propagation on coplanar waveguides: experiment and simulation. *Microwave and Guided Wave Letters, IEEE*, 1(7):161 –163, july 1991.

[51] D. Grischkowsky, Søren Keiding, Martin van Exter, and Ch. Fattinger. Far-infrared time-domain spectroscopy with terahertz beams of dielectrics and semiconductors. *J. Opt. Soc. Am. B*, 7(10):2006–2015, Oct 1990.

[52] L.A. Samoska. An overview of solid-state integrated circuit amplifiers in the submillimeter-wave and thz regime. *Terahertz Science and Technology, IEEE Transactions on*, 1(1):9 –24, sept. 2011.

[53] A. Patrovsky and K. Wu. Active 60 ghz front-end with integrated dielectric antenna. *Electronics Letters*, 45(15):765 –766, 16 2009.

[54] L.-K. Yeh, C.-Y. Chen, and H.-R. Chuang. A millimeter-wave cpw cmos on-chip bandpass filter using conductor-backed resonators. *Electron Device Letters, IEEE*, 31(5):399 –401, may 2010.

[55] M.-R. Nezhad-Ahmadi, M. Fakharzadeh, B. Biglarbegian, and S. Safavi-Naeini. High-efficiency on-chip dielectric resonator antenna for mm-wave transceivers. *Antennas and Propagation, IEEE Transactions on*, 58(10):3388 –3392, oct. 2010.

[56] W. Heinrich. The flip-chip approach for millimeter wave packaging. *Microwave Magazine, IEEE*, 6(3):36 – 45, sept. 2005.

[57] F. Alessandri, W. Menzel, M. Mongiardo, and R. Sorrentino. Efficient full-wave analysis of coplanar waveguide to slotline interconnections with finite metallization thickness accounting for air bridge effects. In *Microwave Symposium Digest, 1994., IEEE MTT-S International*, pages 875 –878 vol.2, may 1994.

[58] Yo-Shen Lin and Chun Hsiung Chen. Design and modeling of twin-spiral coplanar-waveguide-to-slotline transitions. *Microwave Theory and Techniques, IEEE Transactions on*, 48(3):463 –466, mar 2000.

[59] K. Hettak, N. Dib, A. Sheta, A.A. Omar, G.-Y. Delisle, M. Stubbs, and S. Toutain. New miniature broadband cpw-to-slotline transitions. *Microwave Theory and Techniques, IEEE Transactions on*, 48(1):138 –146, jan 2000.

[60] J. Naylor, T. Weller, M. Smith, and J. Culver. Slow-wave cpw slot-line transition. *Microwaves, Antennas and Propagation, IEE Proceedings*, 152(5):297 – 298, oct. 2005.

[61] K.-P. Ma, Y. Qian, and T. Itoh. Analysis and applications of a new cpw-slotline transition. *Microwave Theory and Techniques, IEEE Transactions on*, 47(4):426 – 432, apr 1999.

[62] Kuang-Ping Ma and T. Itoh. A new broadband coplanar waveguide to slotline transition. In *Microwave Symposium Digest, 1997., IEEE MTT-S International*, volume 3, pages 1627 –1630 vol.3, jun 1997.

[63] R. E. Collin and R. F. Zucker. *Antenna Theory, Part II*. NewYork: McGraw-Hill, 1969.

[64] Constantine A. Balanis. *Modern Antenna Handbook*. John Wiley & Sons, Inc., 2008.

[65] M. Lange and J. Detlefsen. 94 ghz three-dimensional imaging radar sensor for autonomous vehicles. *Microwave Theory and Techniques, IEEE Transactions on*, 39(5):819 –827, may 1991.

[66] A.J. Martinez-Ros, J.L. Gomez-Tornero, and G. Goussetis. Microstrip half-mode leaky-wave antenna operating at 94 ghz. In *Microwave Workshop Series on Millimeter Wave Integration Technologies (IMWS), 2011 IEEE MTT-S International*, pages 45 –48, sept. 2011.

[67] Ning Yang, C. Caloz, and K. Wu. Full-space scanning periodic phase-reversal leaky-wave antenna. *Microwave Theory and Techniques, IEEE Transactions on*, 58(10):2619 –2632, oct. 2010.

[68] M.R.M. Hashemi and T. Itoh. Evolution of composite right/left-handed leaky-wave antennas. *Proceedings of the IEEE*, 99(10):1746 –1754, oct. 2011.

[69] M. Garcia-Vigueras, J.L. Gomez-Tornero, G. Goussetis, A.R. Weily, and Y.J. Guo. Enhancing frequency-scanning response of leaky-wave antennas using high-impedance surfaces. *Antennas and Wireless Propagation Letters, IEEE*, 10:7 –10, 2011.

[70] A. Salman. The millimeter wave radiation of a dielectric leaky-wave antenna coupled with a diffraction grating for the broadside radiation: Narrow-face interaction. *Journal of Infrared, Millimeter and Terahertz Waves*, 31:1032–1047, 2010.

[71] W.M. Abdel-Wahab, D. Busuioc, and S. Safavi-Naeini. Millimeter-wave high radiation efficiency planar waveguide series-fed dielectric resonator antenna (dra) array: Analysis, design, and measurements. *Antennas and Propagation, IEEE Transactions on*, 59(8):2834 –2843, aug. 2011.

[72] F.K. Schwering and Song-Tsuen Peng. Design of dielectric grating antennas for millimeter-wave applications. *Microwave Theory and Techniques, IEEE Transactions on*, 31(2):199 –209, feb. 1983.

[73] H.F. Hammad, Y.M.M. Antar, A.P. Freundorfer, and M. Sayer. A new dielectric grating antenna at millimeter wave frequency. *Antennas and Propagation, IEEE Transactions on*, 52(1):36 – 44, jan. 2004.

[74] A.S. Al-Zoubi, A.A. Kishk, and A.W. Glisson. A linear rectangular dielectric resonator antenna array fed by dielectric image guide with low cross polarization. *Antennas and Propagation, IEEE Transactions on*, 58(3):697 –705, march 2010.

[75] A.S. Abdellatif, M. Basha, and S. Safavi-Naeini. Low-cost and high-efficiency multi-beam antenna for millimeter-wave applications. *Antennas and Wireless Propagation Letters, IEEE*, 11:141 –143, 2012.

[76] Jianming Dai, Jiangquan Zhang, Weili Zhang, and D. Grischkowsky. Terahertz time-domain spectroscopy characterization of the far-infrared absorption and index of refraction of high-resistivity, float-zone silicon. *J. Opt. Soc. Am. B*, 21(7):1379–1386, Jul 2004.

[77] Yongmei Pan and Shanjia Xu. A new dielectric grating antenna with large leakage constant for millimeter-wave applications. *International Journal of Infrared and Millimeter Waves*, 28:345–353, 2007.

[78] F. Marty, L. Rousseau, B. Saadany, B. Mercier, O. Franais, Y. Mita, and T. Bourouina. Advanced etching of silicon based on deep reactive ion etching for silicon high aspect ratio microstructures and three-dimensional micro- and nanostructures. *Microelectronics Journal*, 36(7):673 – 677, 2005.

[79] S. Paulotto, P. Baccarelli, F. Frezza, and D.R. Jackson. A novel technique for open-stopband suppression in 1-d periodic printed leaky-wave antennas. *Antennas and Propagation, IEEE Transactions on*, 57(7):1894 –1906, july 2009.

[80] M. Navarro-Tapia, J. Esteban, and C. Penalosa. On the actual possibilities of applying the composite right/left-handed waveguide technology to slot array antennas. *Antennas and Propagation, IEEE Transactions on*, PP(99):1, 2012.